ISSN 0915-633X

NATIONAL INSTITUTE FOR FUSION SCIENCE

Enstrophy Generation in a Shock-Dominated Turbulence

H. Miura

(Received - Aug. 23, 1995)

NIFS-372 Sep. 1995

RESEARCH REPORT
NIFS Series

NAGOYA, JAPAN

Enstrophy Generation in a Shock-Dominated Turbulence

Hideaki MIURA

Theory and Computer Simulation Center,

National Institute for Fusion Science,

Nagoya 464-01, JAPAN

A mechanism of enstrophy generation is investigated numerically in a shock-dominated turbulence driven by a random external force which has only the compressible component. Enstrophy is generated, especially on collision of shock, as a pair of vortex tube of opposite sense of rotation behind curved shocks. The roles of various terms in enstrophy equation are clarified in enstrophy generation process. Generation of enstrophy is enhanced by strong alignment of each term of the enstrophy equation with the vorticity vector.

KEYWORDS:compressible fluid, shock, turbulence, vorticity generation, vortex pair, baroclinic term, alignment of the vorticity vector

§1. Introduction

Organized vortical structures such as vortex tubes and layers often play significant roles in turbulence dynamics in incompressible turbulence.[1, 2] In a compressible turbulence, the tube and layer structures of vortices also manifest themselves when the rotational component of the fluid velocity is not small.[3, 4] A transition of vortex structure from a layer to a tube due to the Kelvin-Helmholtz instability was observed by Porter et al.[4] in their 512^3 numerical simulation of an inviscid compressible flow, which is similar to that in an incompressible flow (see Kishiba et al[5]). When the compressive component of velocity is substantial, shocks (dilatational motions) take part in the dynamics in addition to vortical motions. Interactions between shocks and vortical motions then make the flow field quite complicated. Shocks are distorted by vortical motions, which in turn leads to further generation of vorticity due to curvature effects.[6, 3] The strength of these interactions depends on relative magnitude of the dilatational and the vortical components of motion. The interaction may be strongest when these two components are comparable. Actually, in a compressible mixing layer, vortical structures are less organized when the convective Mach number becomes closer to unity.[7] It was reported that the compressibility effect may reduce the growth rate of turbulence kinetic energy in a shear flow. See Sarkar[8] and references therein.

The interaction between shocks and turbulence has been investigated by many researchers. The growth rate of turbulence kinetic energy was shown to be suppressed when a turbulence passes through a planer shock front.[9] The baroclinic generation of enstrophy across a bow-shaped shock was analyzed using the Rankine-Hugoniot relation.[6, 3] The property of compressible turbulence may be different depending on the relative magnitude of the dilatational and the vortical components. In most of the above-mentioned work, a vortex-dominated turbulence was considered. Here, on the contrary, we deal with turbulence in which the dilatational motions dominate the vortical ones in order to investigate the mechanism of vorticity generation by shocks. A shock-dominated turbulence is excited by a random force which has only the

compressive component. We try to answer the following questions. (1) What kind of vortical structure is generated in shock-vortex interactions ? (2) How does each term in the vorticity equation contribute to the enstrophy generation ?

An outline of the simulation is described and some physical quantities are introduced in §2. Formation of organized structures in the flow field is described in §3. It is shown that shocks are generated, which in turn generate vorticity in their behind. A mechanism of vorticity generation is investigated by a statistical approach in §4. The dynamical role of each term in the vorticity and the enstrophy equations is studied. Concluding remarks are given in §5.

§2. Overview of numerical results

2.1 Basic equations and numerical simulation

The motion of a compressible viscous fluid may be described by the equations of continuity, momenta and total energy as

$$\frac{\partial \rho}{\partial t} = -\frac{\partial (\rho u_i)}{\partial x_i}, \tag{1}$$

$$\frac{\partial (\rho u_i)}{\partial t} = -\frac{\partial (\rho u_i u_j)}{\partial x_j} - \frac{\partial p}{\partial x_i} + \frac{2}{Re_0}\frac{\partial}{\partial x_j}\left\{ S_{ij} - \frac{1}{3}\delta_{ij}\left(\frac{\partial u_k}{\partial x_k}\right)\right\} + \rho f_i, \quad (i = 1,2,3) \tag{2}$$

$$\frac{\partial E_{\mathrm{T}}}{\partial t} = -\frac{\partial}{\partial x_i}[(E_{\mathrm{T}} + p)u_i] + \frac{1}{{M_0}^2 Pr_0 Re_0(\gamma - 1)}\frac{\partial^2 T}{\partial x_i \partial x_i} + \frac{2}{Re_0}\frac{\partial}{\partial x_j}\left\{ u_i\left[S_{ij} - \frac{1}{3}\delta_{ij}\left(\frac{\partial u_k}{\partial x_k}\right)\right]\right\} + \rho u_i f_i, \tag{3}$$

where ρ is the density, u_i is the i-th component of velocity, p is the pressure,

$$S_{ij} = \frac{1}{2}\left(\frac{\partial u_i}{\partial x_j} + \frac{\partial u_j}{\partial x_i}\right) \tag{4}$$

is the rate of strain tensor, f_i is the i-th component of an external force, E_{T} is the total energy, T is the fluid temperature and γ is the ratio of the specific heats at constant pressure C_{p} and at constant volume C_{v}. The fluid obeys the equation of an ideal gas as

$$p = \frac{1}{\gamma M_0^2}\rho T. \tag{5}$$

The internal and the total energies are expressed as

$$E_{\rm I} = \frac{p}{\gamma - 1}, \tag{6}$$

$$E_{\rm T} = E_{\rm K} + E_{\rm I} = \frac{1}{2}\rho u_i u_i + \frac{p}{\gamma - 1}. \tag{7}$$

Here, we have assumed for simplicity the bulk viscosity be zero and the shear viscosity μ be constant. All the physical quantities have been non-dimensionalyzed in terms of typical density ρ_0, velocity u_0 and length l_0. There are three control parameters, that is, reference Reynolds number $Re_0 = \rho_0 u_0 l_0/\mu$, Prandtl number $Pr_0 = C_{\rm p}\kappa/\mu$ and Mach number $M_0 = u_0/c_0$, where κ is the diffusion coefficient and $c_0 = \sqrt{T_0/M_0^2}$ is the speed of sound.

Equations (1)-(7) are solved numerically by the pseudo-spectral/Runge-Kutta-Gill scheme. Aliasing interactions appearing in the pseudo-spectrum method are not removed completely. Instead, Fourier components of $|\boldsymbol{k}| \geq N/2$ are discarded, N being the number of grid points in one direction. Control parameters are set to be $Re_0 = 200$, $Pr_0 = 0.7$ and $M_0 = \sqrt{2}$. The time increment is set to be $\Delta t = 0.05$. The number of grid points is $N^3 = 64^3$. An external force is given at every time step in the Fourier components at $k_i = 1, 2$ and 3, k_i being the wavenumber in x_i-direction, with a random phase and a constant amplitude . In the present simulation the random force has only the compressive component, i.e. $\nabla \times \boldsymbol{f} = 0$. The simulation starts with a stationary state. Therefore, only irrotational motions are primarily excited, while vortical motions are generated secondarily through nonlinear interactions of irrotational motions. For details of the numerical method, including implementation of a random force, see Kida and Orszag.[10)]

2.2 Physical quantities

The kinetic energy is an indicator of flow activity. The compressive and the rotational components of kinetic energy represent the dilatational and the vortical motions, respectively. These two components are obtained by the Helmholtz decomposition of $\sqrt{\rho}\boldsymbol{u}$ in the Fourier

space.[10, 11] This definition of the decomposition is adopted in order to include effects of density change explicitly. The time-developments of the two components of kinetic energy are shown in Fig.1(a). The compressive component is about 100 times larger than the rotational one throughout the simulation. The compressive component increases at first, attains the maximum around $t \simeq 50$, then goes down to a statistically steady state by $t \simeq 70$. The kinetic energy lost during $50 \leq t \leq 70$ is absorbed into the internal energy to cause an increase of the fluid temperature. A rapid oscillation of the compressive component in Fig.1(a) comes from the energy-exchange mechanism between the kinetic and the internal energies through the pressure work (cf. Miura and Kida[11]). In fact, the compressive component oscillates with period $T_{\mathrm{k}} \simeq 2.9$, which coincides well with the oscillation period of the pressure dilatation term $\langle p\nabla \cdot \boldsymbol{u} \rangle$ (figure is omitted).

The time-variation of the compressive component of kinetic energy may be understood as follows. Lower-wavenumber components of the compressive component of kinetic energy grow rapidly at first because dilatational motions are driven directly by an external force. The lower-wavenumber components continue to grow while some of the energy is being transferred to higher wavenumbers by the nonlinear interactions. The kinetic energy keeps growing until the dilatation dissipation becomes comparable with the energy-input by an external force. Since the dilatation dissipation keeps increasing, the kinetic energy turns to decrease. In the mean time, the dilatation dissipation and the energy-input by an external force balance each other and the fluid motion enters to a statistically steady state.

The kinetic energy spectra which represent the scale distribution of activity of the fluid motion may serve as an indicator of accuracy of the numerical simulation. We plot in Fig.1(b) the mean kinetic energy spectra averaged over $30 \leq t \leq 60$ (an active period) and $80 \leq t \leq 200$ (a statistically steady period). It is seen that the compressive component decays almost algebraically in the both period, implying that the resolution of the simulation is marginal. The rotational component decreases also algebraically at large wavenumbers upto $k \simeq 15$ in

the active period and upto $k \simeq 10$ in the steady period. The rise of the spectrum at larger wavenumbers may be attributed to the aliasing interactions. This part will be discarded in drawing isosurfaces of the enstrophy density in the following sections.

The importance of dilatational motions may be represented by the turbulence Mach number

$$M_{\mathrm{t}} = \sqrt{\left\langle \left(\frac{|\boldsymbol{u}|}{c} \right)^2 \right\rangle}, \tag{8}$$

where $c = \sqrt{T}$ is a local speed of sound. Hereafter, brackets $\langle \ \ \rangle$ are used for the volume-average and an overbar $\overline{\ \ }$ for the time-average. The mean values of M_{t} averaged over $30 \leq t \leq 60$ and $80 \leq t \leq 200$ are 0.15 and 0.08, respectively. Although M_{t} is less than unity in average, local maxima of the Mach number exceed unity, as will be seen later (§3.1).

Turbulence Reynolds number is defined by

$$Re = \sqrt{\frac{5Re_0}{3\epsilon}} \langle \rho \rangle \left\langle |\boldsymbol{u}|^2 \right\rangle, \tag{9}$$

where

$$\epsilon = \epsilon_{\mathrm{C}} + \epsilon_{\mathrm{R}} = \frac{1}{Re_0} \left(\frac{4}{3} \left\langle |\nabla \cdot \boldsymbol{u}|^2 \right\rangle + \left\langle |\boldsymbol{\omega}|^2 \right\rangle \right) \tag{10}$$

is the energy dissipation rate and

$$\boldsymbol{\omega} = \nabla \times \boldsymbol{u} \tag{11}$$

is the vorticity. The first term of eq.(10), which is called the dilatation dissipation rate, represents the additional dissipation peculiar to compressible turbulence.[12, 13] In the present simulation the dilatation dissipation rate occupies 97% of the total. This is extremely opposite to a nearly incompressible flow in which the dilatational dissipation is negligibly small (cf. Case I simulation of Kida and Orszag[10]). Time-averages of Re over $30 \leq t \leq 60$ and over $80 \leq t \leq 200$ yield $\overline{Re} \simeq 11.6$ and 8.0, respectively. Since $\overline{Re}$ is relatively small, a tube structure of vortices, which is known to be formed as the result of the Kelvin-Helmholtz instability for a vortex sheet in a high-Reynolds number turbulence, is rarely observed in the present simulation.

Time-developments of the enstrophy (thin solid line) as well as the maximum (thin dashed line with positive values), the minimum (thin dashed line with negative values) and the mean

square (thick solid line) of dilatation are plotted in Fig.2(a). The enstrophy is nearly zero until $t \simeq 25$, then begins to grow up rapidly, and keeps growing until $t \simeq 68$ at which it takes a maximum, then decays with decaying speed proportional to $t^{-1.9}$ (see Fig.2(b)). We have no clear-cut explanations to this power, however. Every peak of the enstrophy (which is indicated by an arrow in Fig.2(a)) has a corresponding strong surge of maxima and minima of dilatation. By looking carefully at the flow field, we have confirmed that these surges appear when a collision of shocks is taking place (see §3.2 below). It is interesting to note that the growth and the decay in enstrophy occur later than those in the mean square of dilatation. This suggests that enstrophy is generated by dilatational motions which are directly driven by a random force. In the following analysis we concentrate on period $t < 100$ since we are interested in the active generation of enstrophy in $t < 68$ ($= t_c$, say) and sudden reduction of the generation around $t \simeq t_c$.

§3. Formation of coherent structures

3.1 Formation of shock surfaces and vorticity generation

One of the characteristic features of compressible turbulence is that strong vorticity is generated behind shocks. Figure 3 shows isosurfaces of dilatation and enstrophy density at $t = 28.5$. The grey isosurfaces represent the dilatation with a large negative value (shocks), the threshold of which is minus twice of the standard deviation of dilatation. The blue (red) isosurfaces represent enstrophy density with $\omega_2 < 0$ (> 0), the threshold of which is twice of the standard deviation of enstrophy density above the mean value. High-vorticity regions appear typically as a vortex pair behind a curved shock. Two vortex pairs, which consist of blue and red isosurfaces respectively, are observed in Fig.3: One is located at upper-left side attached to a long shock surface, and the other around the center behind another shock.

In Fig.4, we draw contours of local Mach number around the shock located at the center of

Fig.3. The local Mach number is defined by $|\boldsymbol{u}-\boldsymbol{v}_d|/c$ where $\boldsymbol{v}_d$ is the traveling velocity of the shock which is estimated at the top of the bow-shaped contour, i.e. at $(x_1, x_3) \simeq (29, 39)$ in Fig.4. Supersonic regions are shaded. Thick contours show large negative dilatation. The thick bow-shaped contours move upward in Fig.4 (rightward in Fig.3). The fluid is therefore subsonic in front of the dilatation contours and supersonic behind them. The local Mach number on this shock is about 1.1.

The vortex pair observed around the center in Fig.3 is enlarged in Fig.5, which is cut by a plane parallel to the (x_1, x_3)-plane. The high-vorticity region is composed of a vortex pair with blue and red colors behind the shock surface. The vorticity lines depicted by yellow in Fig.5(a) run along the shock surface, which suggests that the vortex pair has been generated by the baroclinic effect as follows.

As is well-known, a curved shock can generate vorticity (Crocco's theorem[14]). An analysis based on the Runkine-Hugoniot relation for an inviscid compressible fluid[3] gives an expression of the vorticity generated behind a shock, in a curvilinear coordinate system (q_1, q_2, q_3), as

$$\boldsymbol{\omega}^{(2)} = A\left(-\frac{u_3^{(1)}}{h_3}\frac{\partial h_3}{\partial q_1}\boldsymbol{e}_2 + \frac{u_2^{(1)}}{h_2}\frac{\partial h_2}{\partial q_1}\boldsymbol{e}_3\right), \tag{12}$$

$$A = \frac{1}{h_1}\frac{4\left(M_s^2-1\right)^2}{(\gamma+1)M_s^2\left[(\gamma-1)M_s^2+2\right]}. \tag{13}$$

Here $\boldsymbol{e}_j$ $(j=1,2,3)$ is the unit vector in the q_j-direction, $\boldsymbol{e}_1$ being normal to the shock surface, h_j is the metric for the q_j-direction, M_s is the Mach number in front of the shock, and the superscripts $^{(1)}$ and $^{(2)}$ denote the quantities in front of and behind the shock, respectively. In the case of a spherical shock, the coordinate system is given by $(q_1, q_2, q_3) = (r, \theta, \phi)$ and $(h_1, h_2, h_3) = (1, r, r\sin\theta)$. Then the vorticity generated behind a spherical shock may be expressed as

$$\boldsymbol{\omega}^{(2)} = \frac{A}{r}\left(-u_\phi^{(1)}\boldsymbol{e}_\theta + u_\theta^{(1)}\boldsymbol{e}_\phi\right), \tag{14}$$

which clearly runs along the shock surface in an anti-clockwise direction facing the back side of the shock. This explains the topological structure of vortex lines and the sense of rotation

of a vortex pair observed in Fig.4.

Since regions with large negative dilatation (shocks) travel much faster than high-vorticity regions, the latter are likely to be left behind the shocks. Once a lump of the high-enstrophy density (in many case it is or was a vortex pair) leaves from a shock surface, it decays rapidly. In Figs.6, we draw isosurfaces of large negative dilatation (grey), high-enstrophy with $\omega_2 > 0$ (blue) and with $\omega_2 < 0$ (red) at three consecutive times. A high-enstrophy density region extended horizontally in the bottom in Fig.6, which is left apart from a shock, shrinks rapidly as time goes on, while portions of the other blue and red isosurfaces, which are attached to shocks surfaces, keep their magnitudes because of continual generation of enstrophy by curved shocks. This behavior of the time-development of high-enstrophy regions is typically observed in active period ($t < t_c$). It suggests that when there is no special source of the enstrophy density such as shock collisions or curved shocks, vortical motion is weakened rapidly by the viscous effect. We note here that behavior of enstrophy lumps are somewhat different in the period when the enstrophy decays slowly ($t > t_c$). In $t > t_c$, many of enstrophy lumps, which are apart from shocks, live longer times. As will be seen in the next section, contribution of the viscous effect to decrease the enstrophy becomes smaller as the enstrophy decays.

3.2 Collision of shocks

In the present simulation, shocks collide with each other from time to time. Each collision may be identified with a steep peak in variation of dilatation (see Fig.2(a)). A strong collision of shocks happens to occur at $t \simeq t_c$. In Figs.7(a) and (b), we draw isosurfaces of dilatation with a large negative values before ($t = 67.3$) and after ($t = 68.8$) the collision, respectively. To make the shock structure clear, each shock was rimmed. In Fig.7(a), there are three well-defined shock surfaces denoted by A, B and C, each of which travels in the direction denoted by arrows. Around the center, shocks A and B are about to make a head-on collision. These two shocks are intersecting almost orthogonally with shock C.

In Fig.8(a), we overlay isosurfaces of high-enstrophy density on Fig.7(b). It is seen that high-enstrophy density is generated around the center, i.e., behind all of the three shock surfaces. We observe also a pair of lumps of high-enstrophy density right to the center (in front of a shock), each of which rotates in opposite sense. We have checked that this vortex pair has been generated before by another collision of shocks. Figure 8(b) is a magnification of the region bounded by three shocks in Fig.8(a). There are several pairs (blue and red) of high-enstrophy density behind shocks. There is one along a curved shock in the left of the shock-bounded region. A pair of blue and red vortices at the top are portions of large isosurfaces. In the right, a large lump of blue isosurface constitutes a vortex pair with a large red isosurface behind it. Finally, in the upper-right, outside the shock-bounded region, there is another vortex pair. From these observations, we conclude that a typical structure of vorticity generated by collisions of shocks is a vortex pair.

§4. Enstrophy budget

4.1 Vorticity and enstrophy equations

In order to clarify the generation mechanism of vorticity observed in previous sections, we investigate contributions of various terms of vorticity equation

$$\frac{\partial \boldsymbol{\omega}}{\partial t} = -\nabla \times [(\boldsymbol{u}\cdot\nabla)\boldsymbol{u}] + \frac{\nabla\rho\times\nabla p}{\rho^2} + \frac{1}{Re}\frac{\nabla^2\boldsymbol{\omega}}{\rho} - \frac{1}{Re}\frac{\nabla\rho\times\left[\nabla^2\boldsymbol{u}+\frac{1}{3}\nabla(\nabla\cdot\boldsymbol{u})\right]}{\rho^2}, \quad (15)$$

and enstrophy density equation

$$\frac{\partial Q}{\partial t} = -\boldsymbol{\omega}\cdot\{\nabla\times[(\boldsymbol{u}\cdot\nabla)\boldsymbol{u}]\} + \boldsymbol{\omega}\cdot\frac{\nabla\rho\times\nabla p}{\rho^2} + \frac{1}{Re}\frac{\boldsymbol{\omega}\cdot\nabla^2\boldsymbol{\omega}}{\rho} - \frac{1}{Re}\frac{\boldsymbol{\omega}\cdot\left\{\nabla\rho\times\left[\nabla^2\boldsymbol{u}+\frac{1}{3}\nabla(\nabla\cdot\boldsymbol{u})\right]\right\}}{\rho^2}, \quad (16)$$

where

$$Q = \frac{1}{2}|\boldsymbol{\omega}|^2 \quad (17)$$

is the enstrophy density. Taking a spatial average of eq.(16), we obtain

$$\frac{d\langle Q\rangle}{dt} = -\langle\boldsymbol{\omega}\cdot\{\nabla\times[(\boldsymbol{u}\cdot\nabla)\boldsymbol{u}]\}\rangle+\left\langle\boldsymbol{\omega}\cdot\frac{\nabla\rho\times\nabla p}{\rho^2}\right\rangle +\frac{1}{Re}\left\langle\frac{\boldsymbol{\omega}\cdot\nabla^2\boldsymbol{\omega}}{\rho}\right\rangle-\frac{1}{Re}\left\langle\frac{\boldsymbol{\omega}\cdot\left\{\nabla\rho\times\left[\nabla^2\boldsymbol{u}+\frac{1}{3}\nabla(\nabla\cdot\boldsymbol{u})\right]\right\}}{\rho^2}\right\rangle. \tag{18}$$

Each term in the rhs. of eq.(18) is called the rotational, the baroclinic, the viscous and the viscous-compression terms in order.

Time-developments of these four terms are shown in Fig.9 for $t \leq 100$. All terms are small until $t \simeq 25$. But around $t \simeq 25$, the baroclinic (thick solid line) and the viscous-compression (thick dashed line) terms begin to increase faster than the others. This is because these two terms contain $\nabla\rho$ as a factor and are linear in $\boldsymbol{\omega}$ (while the others are quadratic in $\boldsymbol{\omega}$). In period $25 \leq t \leq 75$, the viscous-compression and the baroclinic terms play a dominant role in vorticity generation while the viscous term (thick dotted line) opposes it. These three terms show sometimes steep peaks simultaneously, which synchronize with peaks of the dilatation, and therefore with collisions of shocks (cf. Fig.2(a)). The contribution of the rotational term (thin solid line) is quite small. One of the most prominent features in Fig.9 is a sudden reduction in magnitude of the baroclinic, the viscous and the viscous-compression terms around $t \simeq t_c$ when the enstrophy arrives at the maximum (see Fig.2(a)). A mechanism of this reduction will be discussed in the next section. After t_c, the baroclinic and the viscous-compression terms, which are still positive, are reduced in magnitude to the level of the rotational term. While the viscous term retains relatively large negative values, it is also reduced drastically. The reduction of these terms makes the vorticity generation to be inactive after t_c.

The above observations suggest us to divide the period of the present numerical simulation into two parts at t_c, before which the baroclinic and the viscous-compression terms are active in vorticity generation, and after which they become too weak to maintain the enstrophy. In the following we consider the difference in vorticity dynamics before and after t_c.

4.2 *Reduction of vorticity generation*

As seen in Fig.9, the contribution from each term in eq.(18) is reduced around t_c. We consider here how the large vorticity generation is sustained before t_c and what is the reason of the sudden reduction around t_c.

Equation (18) is rewritten, by expressing the vector products explicitly, as

$$\frac{d\langle Q\rangle}{dt} = -\langle|\boldsymbol{\omega}|\cdot|\nabla\times[(\boldsymbol{u}\cdot\nabla)\boldsymbol{u}]|\cos\theta_r\rangle + \left\langle|\boldsymbol{\omega}|\cdot\left|\frac{\nabla\rho\times\nabla p}{\rho^2}\right|\cos\theta_b\right\rangle + \frac{1}{Re}\left\langle|\boldsymbol{\omega}|\cdot\left|\frac{\nabla^2\boldsymbol{\omega}}{\rho}\right|\cos\theta_v\right\rangle + \frac{1}{Re}\left\langle|\boldsymbol{\omega}|\cdot\left|\frac{\nabla\rho\times\left[\nabla^2\boldsymbol{u}+\frac{1}{3}\nabla(\nabla\cdot\boldsymbol{u})\right]}{\rho^2}\right|\cos\theta_{vc}\right\rangle, \quad (19)$$

where θ_r, θ_b, θ_v and θ_{vc} are respectively the angles that the rotational, the baroclinic, the viscous and the viscous-compression terms make with the vorticity vector. Notice that the magnitude of each term in eq.(19) depends not only on the magnitude of the corresponding term in eq.(15) but also on the probability distribution of the above angles. Therefore the reduction of each term in eq.(18) may be caused by the reduction in magnitude and by uniformalization in distributions of these angles. We investigate below these two possibilities.

4.2.1 *Magnitude of each term in the vorticity equation*

The time-evolutions of the root-mean-squares of the rotational (thin solid line), the baroclinic (thick solid line), the viscous (thick dotted line) and the viscous-compression (thick dashed line) terms are compared in Fig.10. All of them are reduced in magnitude around t_c. The reduction in magnitude of the baroclinic and the viscous-compression terms is attributed to the reduction of the compressive component of kinetic energy (Fig.1(a)) because $\nabla\rho$, ∇p and $\nabla(\nabla\cdot\boldsymbol{u})$ become small then. On the other hand, the reduction of the rotational and the viscous terms is a result of the reduction of the vorticity magnitude because they are linear in $\boldsymbol{\omega}$. (Note that the rotational term in eq.(15) may be expressed as $\nabla\times[(\boldsymbol{u}\cdot\nabla)\boldsymbol{u}] = (\boldsymbol{u}\cdot\nabla)\boldsymbol{\omega}+\boldsymbol{\omega}(\nabla\cdot\boldsymbol{u})-(\boldsymbol{\omega}\cdot\nabla)\boldsymbol{u}$.)

A key observation important in the following discussion is that relative magnitude of the four terms in Fig.10 is different from that in Fig.9. While the rotational term is the largest in

Fig.10, contribution of this term to the enstrophy generation in Fig.9 is small. On the contrary, the viscous term takes large negative values in Fig.9 in period $25 \leq t \leq t_c$, whereas it is the smallest in Fig.10. These features suggest the importance of the probability distribution of angles between the vorticity vector and these terms in estimating the contribution to enstrophy generation.

4.2.2 Alignment of the vorticity vector

Motivated by the above discussion, we examine probability density function (pdf) $P(\theta)$ for $\theta = \theta_r, \theta_b, \theta_v$ and θ_{vc}. We compare it with an $|\boldsymbol{\omega}|^2$-weighted pdf, denoted by $P_\omega(\theta)$, in order to study the contribution from high-vorticity regions. (We also calculated a $|\nabla \cdot \boldsymbol{u}|^2$-weighted pdf, which turned out to be similar to $|\boldsymbol{\omega}|^2$-weighted ones.)

The pdfs, $P(\theta_r)$ and $P_\omega(\theta_r)$, of the angles between the vorticity and the rotational term are shown in Figs.11(a) and (b), respectively. The contour levels are higher in darker regions. The resolution of these contours is 180 in the ordinate and 1,000 in the abscissa. It is seen in Fig.11(a) that $P(\theta_r)$ has two peaks around $\theta_r = 0°$ and 180° in $t < 20$ while there is only one peak around $\theta_r = 180°$ in $20 < t < t_c$. The existence of these peaks is more evident in Fig.11(b), where two peaks around $\theta_r = 0°$ and 180° in $t < 20$ are more clearly seen. Furthermore, in $20 < t < t_c$, another peak appears around $\theta_r = 0°$ which are not observed in Fig.11(a). On the other hand, $P_\omega(\theta_r)$ takes smaller values around $\theta_r \simeq 90°$ than $P(\theta_r)$. Hence, we see that $P_\omega(\theta_r)$ is quite localized around $\theta_r = 0°$ and 180° before t_c and that it is uniform after t_c. These observations lead us to the conclusion that the contribution of the rotational term to the enstrophy generation is small after a volume average because parallel and anti-parallel components cancel out each other both in before and after t_c. It explains the reason why the rotational term in eq.(18) do not play a significant role to the enstrophy generation while magnitude of it in eq.(15) is larger than the other terms.

The localization of $P_\omega(\theta_r)$ around $\theta_r = 0°$ and 180° before t_c may be explained as follows.

The rotational term in eq.(18) can be rewritten as

$$-\langle \boldsymbol{\omega} \cdot \{\nabla \times [(\boldsymbol{u} \cdot \nabla)\boldsymbol{u}]\}\rangle = -\frac{1}{2}\left\langle |\boldsymbol{\omega}|^2 (\nabla \cdot \boldsymbol{u})\right\rangle + \langle \boldsymbol{\omega} \cdot [(\boldsymbol{\omega} \cdot \nabla)\boldsymbol{u}]\rangle . \tag{20}$$

The first and the second terms are called the compression and the vortex-stretching terms, respectively. In the present numerical simulation, the magnitude of the former is about five times larger than that of the latter (figure is not shown). Since the compression term consists of the inner product of $\boldsymbol{\omega}$ and $-\boldsymbol{\omega}\,(\nabla \cdot \boldsymbol{u})$, they are always parallel or anti-parallel according to the sign of the dilatation, which explains the two peaks around $\theta_r = 0°$ and 180°.

Next we consider the baroclinic and the viscous-compression terms. As will be seen below, the pdfs of angles relevant to these two terms are similar. Since ρ, p and $\nabla \cdot \boldsymbol{u}$ obeys the same wave-equation in the acoustic limit, it is reasonable that the baroclinic and the viscous-compression terms behave in a similar way when the flow field is dominated by dilatational motions. The time-developments of $P(\theta_{\rm b})$ and $P(\theta_{\rm vc})$ are shown in Figs.12(a) and (b), respectively. At the very early stage of evolution ($t < 10$), both of them are highly localized around $\theta_{\rm b}, \theta_{\rm vc} = 0°$, showing that the vorticity is almost parallel to the baroclinic and the viscous-compression terms. Since the vorticity generation in this period is mainly caused by these terms (see Fig.9), it is natural for the vorticity vector to be aligned with them. After $t \simeq 25$, both $P(\theta_{\rm b})$ and $P(\theta_{\rm vc})$ are almost uniform. Such uniform distributions seem to conflict with large contributions of these terms to the enstrophy generation seen in Fig.9 because the regions with $\theta_{\rm b}, \theta_{\rm vc} < 90°$ and $> 90°$ should cancel each other after a volume average. However, such a conflict is solved by investigating the $|\boldsymbol{\omega}|^2$-weighted pdf.

The time-developments of $P_\omega(\theta_{\rm b})$ and $P_\omega(\theta_{\rm vc})$ are shown in Figs.13(a) and (b), respectively. The both pdfs have a sharp peak around $\theta_{\rm b}, \theta_{\rm vc} = 0°$ in the early period ($t < 25$), which is similar to Fig.12. In a later period ($25 < t < t_c$), they have two peaks around $\theta_{\rm b}, \theta_{\rm vc} = 0°$ and 180°, which are not observed in Fig.12. Since the peaks around $\theta_{\rm b}, \theta_{\rm vc} = 0°$ are much larger than those around $\theta_{\rm b}, \theta_{\rm vc} = 180°$, the contributions of these two peaks to the enstrophy generation do not cancel. This leads to a large contribution of the baroclinic and the viscous-

compression terms to the enstrophy generation. Hence, the rapid growth of the enstrophy observed before t_c in Fig.2(a) is caused not only by the large magnitude of these two terms but also by an alignment with the vorticity vector. An anti-parallel alignment of the vorticity vector and the two terms occurs either behind curved shocks or tips of shocks. Behind shocks, the density and the pressure oscillate like an acoustic wave, and a phase difference between these two oscillations may cause the reverse of the direction of baroclinic term. Another feature in Figs.13 is a drastic uniformalization of the pdfs. It implies that contribution of the baroclinic and the viscous-compression terms to the enstrophy generation becomes small after t_c when the average is taken over the whole angle. The mechanism of uniformalization around t_c will be discussed in the next section.

Finally, we investigate the pdf of θ_v in order to find the reason why the viscous term takes large negative values in Fig.9 though the magnitude of it in eq.(15) is the smallest of all terms. We plot $P(\theta_v)$ and $P_\omega(\theta_v)$ in Figs.14(a) and (b), respectively. $P(\theta_v)$ has a sharp peak around $\theta_v = 180°$ before t_c, while the peak is gradually broaden after $t \simeq 22$ to be spreaded to $\theta_v = 0°$. A localization of the distribution density of θ_v around 180° is more clearly seen in Fig.14(b). Most of $P_\omega(\theta_v)$ gathers in $\theta_v > 165°$. Such a strong alignment of the vorticity vector and the viscous term causes a rapid decay of the enstrophy lumps which are apart from shocks (see Figs.6). The strong alignment also explains why the viscous term makes a large and negative contribution to the enstrophy generation in Fig.9 whereas magnitude of it is the smallest of the four terms.

While θ_v gathers around 180° at the most of time, temporal uniformalizations of $P(\theta_v)$ and $P_\omega(\theta_v)$ are observed at several times such as $t \simeq 14, 22, 34, 46, 53, 64$ and $68 (= t_c)$. Similar behaviors are also observed simultaneously in Fig.11(b), Fig.13(a) and (b) though they are not so clear as in Fig.14(b). All these uniformalizations synchronize with peaks of the square root of the dilatation in Fig.2(a) and therefore with collisions of shocks. Because of the difference in the traveling velocity, the high-vorticity regions generated by collisions of shocks are left

behind the shocks. The vorticity apart from shocks can orient rather independently from the direction of shocks, which may cause uniform distributions of angles observed above. Note that the uniformalization around t_c are different from others in the sense that the alignment of the vorticity and the four terms are not recovered. The uniformalization of the pdf makes the viscous dissipation of enstrophy inefficient to cause a relatively long life-time of lumps of high-enstrophy density regions after t_c. The mechanism of the eternal uniformalization around t_c will be discussed in the next section.

4.2.3 Uniformalization of angle distributions

Here we consider why the alignment of the vorticity vector with the four terms is lost around t_c to cause uniformalization of distributions of θ_r, θ_b, θ_{vc} and θ_v. Since the vorticity vectors and all of the four terms are aligned in parallel or anti-parallel before t_c at high-vorticity region, there should be a characteristic direction which dominates the flow field. Recall that the vorticity is generated mainly by shocks. As mentioned before, the $|\nabla \cdot \boldsymbol{u}|^2$-weighted pdfs show a similar behavior to the $|\boldsymbol{\omega}|^2$-weighted pdfs. Thus we may as well say that the alignment occurs around shock regions. In the following we consider an alignment of the vorticity vector related to the density gradient which may represent the directions of shocks. A decomposition of the vorticity into parallel and perpendicular components to the density gradient defines corresponding two components of the enstrophy as

$$\langle Q \rangle = \left\langle Q_{\parallel} \right\rangle + 2 \langle Q_{\perp} \rangle , \tag{21}$$

$$\left\langle Q_{\parallel} \right\rangle = \left\langle \left(\boldsymbol{\omega} \cdot \frac{\nabla \rho}{|\nabla \rho|} \right)^2 \right\rangle , \tag{22}$$

$$\langle Q_{\perp} \rangle = \frac{1}{2} \left(\langle Q \rangle - \left\langle Q_{\parallel} \right\rangle \right) . \tag{23}$$

Here the perpendicular component is multiplied by $\frac{1}{2}$ because the degrees of the freedom of this component is twice of the parallel one. The density gradient looses the meaning of the shock direction where the dilatation takes positive or small negative values. Nevertheless, the decomposition of the enstrophy by the density gradient is useful because the orientation of the

baroclinic and the viscous-compression terms (and therefore the vorticity generated by these two terms) depends on the density gradient vector.

In Fig.15(a), we plot the two components of the enstrophy. Before t_c, the perpendicular component of the enstrophy (dashed line) is larger than the parallel component (solid line), while an equipartition of the two components is achieved after t_c. It implies that the vorticity field is aligned tangentially with shocks before t_c while it decorrelates after t_c.

In order to study the alignment effect on the four terms in eq.(15), we decompose them by the use of density gradient. The two components of the viscous term in eq.(18), which are parallel (solid line) and perpendicular (dashed line) to the density gradient, are depicted in Figs.15(b). The perpendicular component is larger than the parallel component before t_c, whereas they equilibrate after t_c. It implies that the viscous term can be aligned tangentially with shocks when the compressibility is strong enough even though it does not contain $\nabla\rho$ explicitly. We note here that the rotational term shows similar behavior with the viscous term. The perpendicular component of the rotational term takes larger values than the parallel one. Note also that the baroclinic and the viscous-compression terms have only perpendicular component because the corresponding two terms in eq.(15) contains outer products of $\nabla\rho$.

From the above results, we may understand the uniformalizations of the angle-distributions around t_c in Figs.11−14 as follows. Before t_c, the vorticity vectors and the four terms are highly aligned as seen in Figs.11−14. This alignment comes from existence of shocks. (Recall that the $|\nabla\cdot\boldsymbol{u}|^2$-weighted pdfs give similar results with $|\boldsymbol{\omega}|^2$-weighted ones. The alignment of the vorticity vector and the four terms occurs at high-dilatation regions as well as high-vorticity regions.) When the compressibility becomes weaker due to the decrease of the compressive component of kinetic energy, the baroclinic and the viscous-compression terms in eq.(15) become weaker (see Fig.10). Since these two terms contribute to generation of $\langle Q_\perp \rangle$, the reduction of the compressibility around t_c directly leads to the reduction of $\langle Q_\perp \rangle$ relative to $\left\langle Q_\parallel \right\rangle$. Based on researches on incompressible homogeneous turbulence, we may expect that direction of the

vorticity vector tends to be decorrelated with shocks when there is no strong mechanism to force the vorticity to be aligned. Consequently, the vorticity tends to orient isotropically to all directions, to cause uniformalization of pdfs in Figs.11–14. To sum up this subsection, strong compressibility causes alignment of the vorticity and the four terms to sustain the large enstrophy generation while the alignment is lost when the compressibility becomes weak enough to cause reduction of the enstrophy generation.

§5. Concluding Remarks

In this article, vorticity generation in a compressible turbulence has been investigated by executing the numerical simulation with an external force which has only the compressive component. It has been shown that the main structure of the vorticity is a vortex pair which is generated by curvature effects and collisions of shocks.

A numerical estimation of contributions of various terms in eq.(18) to the vorticity generation has shown that the viscous-compression term is as important as the baroclinic term when the viscous effect is finite. The decrease of dilatational motions causes the reduction of the enstrophy generation by these two terms in two ways. One is the reduction of the dilatation, density and pressure gradients in magnitude. The other is a uniformalization of angle distributions between the vorticity vector and each term in the vorticity equation. This investigation has revealed that the strong enstrophy generation in the present simulation is sustained by a strong alignment between these terms and the vorticity vector.

Acknowledgments

The author would like to thank Professor S. Kida in Kyoto University for frequent discussions, fruitful suggestions and review of this article.

The numerical simulation presented here was performed on the VP2600 of the Kyoto Uni-

versity. Numerical results obtained by the numerical simulation were visualized with facilities in the National Institute for Fusion Science. This work was partially supported by the Grant-in-Aid for Scientific Research from the Ministry of Education, Science and Culture.

References

1) Z.-S. She, E. Jackson and S. A. Orszag: Nature **344**, 226 (1990).

2) S. Kida and M. Tanaka: J. Fluid Mech. **274**, 43 (1994).

3) H. Miura and S. Kida: J. Phys. Soc. Japan **63**, 4000 (1994).

4) D. H. Porter, A. Pouquet and P. R. Woodward: Phys. Fluids **6**, 2133 (1994).

5) S. Kishiba, K. Ohkitani and S. Kida: J. Phys. Soc. Japan **63**, 2133 (1994).

6) S. Kida and S. A. Orszag: J. Sci. Comput. **5**, 1 (1990).

7) G. S. Elliott, M. M. Samimy and S. A. Arnette: Phys. Fluids **7**, 864 (1994).

8) S. Sarkar: J. Fluid Mech. **282**, 163 (1995).

9) S. Lee, S. K. Lele and P, Moin: J. Fluid Mech. **251**, 533 (1993).

10) S. Kida and S. A. Orszag: J. Sci. Comp. **5**, 85 (1991).

11) H. Miura and S. Kida: Phys. Fluids **7**, 1732 (1994).

12) O. Zeman: Phys. Fluids A **2**, 178 (1990).

13) S. Sarkar, G. Erlebacher, M. Y. Hussaini and H. O. Kreiss: J. Fluid Mech. **227**, 473 (1991).

14) J. D. Anderson Jr., *Modern Compressible Flow with Historical Perspective* (McGraw-Hill, New York, 1990) 2nd ed.

Figure captions

Figure 1 (a) Time-developments of mean values of the compressive (solid line) and the rotational (dashed line) components of kinetic energy. (b) Time-averages of the compressive and rotational components of kinetic energy spectra. White (black) circles are the compressive component of kinetic energy spectrum averaged over $30 \leq t \leq 60$ ($80 \leq t \leq 200$). White (black) boxes are the rotational component of kinetic energy spectrum averaged over $30 \leq t \leq 60$ ($80 \leq t \leq 200$).

Figure 2 (a) Time-developments of the enstrophy (thin solid line), the mean square (thick solid line), maximum (dashed line with positive values) and minimum (dashed line with negative values) of the dilatation. The maximum and minimum values of the dilatation are multiplied by $\frac{1}{3} \times 10^{-4}$ and the mean square value by 10^{-2}. Sharp peaks of the maximum and the minimum values of dilatation correspond to shock-shock collisions. Typical peaks are indicated by arrows. Oscillations of the mean square value of the dilatation come from acoustic waves. (b) A graph of $t^{1.9}\langle Q \rangle$. The graph becomes almost horizontal after $t \simeq 100$, which implies that the enstrophy decays with $t^{-1.9}$ speed.

Figure 3 Isosurfaces of the dilatation (grey) with a large negative value and the enstrophy density (blue and red) with a large positive value. The blue (red) isosurfaces shows the regions in which $\omega_2 < 0$ (> 0). The blue and red isosurfaces constitute vortex pairs behind shocks.

Figure 4 Contours of local Mach number. Thin contours represent local Mach number and a shaded region represents that the flow is supersonic. Thick contours show the dilatation with large negative values (shock). The flow is supersonic (subsonic) in front of (behind) the bow-shaped shock, which travels upward.

Figure 5 A magnification of a vortex pair observed in Fig.3. Vortex lines are shown with yellow lines. Vortex lines come from the left side, turn to the right and go into the paper.

Figure 6 Isosurfaces of the dilatation and the enstrophy density at (a) $t = 39.0$, (b) $t = 39.3$ and (c) $t = 39.5$. A portion of blue isosurface which lies horizontally in Fig.6(a) fades away gradually in (b) and (c).

Figure 7 Schematic pictures of shocks (a) before ($t = 67.3$) and (b) after ($t = 68.8$) a collision. Shocks travel to the direction of arrows. Shocks A and B collide face to face while they are intersecting shock C almost orthogonally.

Figure 8 (a) Shocks (light grey) and high-enstrophy regions (dark grey) are drawn simultaneously at $t = 68.8$. High-enstrophy regions are generated behind shocks A, B and C. (b) Magnification of (a). There are several pairs of blue ($\omega_2 < 0$) and red ($\omega_2 > 0$) vortices observed inside as well as outside of shock-walls (grey).

Figure 9 Contributions of four terms of the enstrophy equation to the enstrophy budget in period $t \leq 100$. The baroclinic (thick solid line) and the viscous-compression (dashed line) terms generate enstrophy, while the viscous term (dotted line) dissipates it. The rotational term (thin solid line) does not play a significant role.

Figure 10 Comparison in magnitude of the rotational (thin solid line), the baroclinic (thick solid line), the viscous (dotted line) and the viscous-compression (dashed line) terms in the rhs. of the vorticity equation.

Figure 11 Contours of (a) pdf and (b) the $|\omega|^2$-weighted pdf of angle θ_r. Contour levels are and 10^{-4}, 3×10^{-3}, 7×10^{-3}, 10^{-2} and 3×10^{-2}. Levels 10^{-4} and 3×10^{-2} are not observed in (a). The contour levels are higher in the darker regions.

Figure 12 Contours of (a)$P(\theta_r)$ and (b)$P(\theta_{vc})$. Levels and shades of contours are the same with Figs.11.

Figure 13 Contours of the $|\omega|^2$-weighted pdfs of (a)θ_r and (b)θ_{vc}. Contour levels are 10^{-4}, 3×10^{-3}, 10^{-2} and 3×10^{-2} (higher in the darker regions).

Figure 14 Contours of (a) pdf and (b) the $|\omega|^2$-weighted pdf of angle θ_v. Contour levels are the same with Figs.13.

Figure 15 Decomposition of (a) the enstrophy and (b) the viscous term into parallel (solid line) and perpendicular components (dashed line) to the density gradient. The perpendicular components are halved.

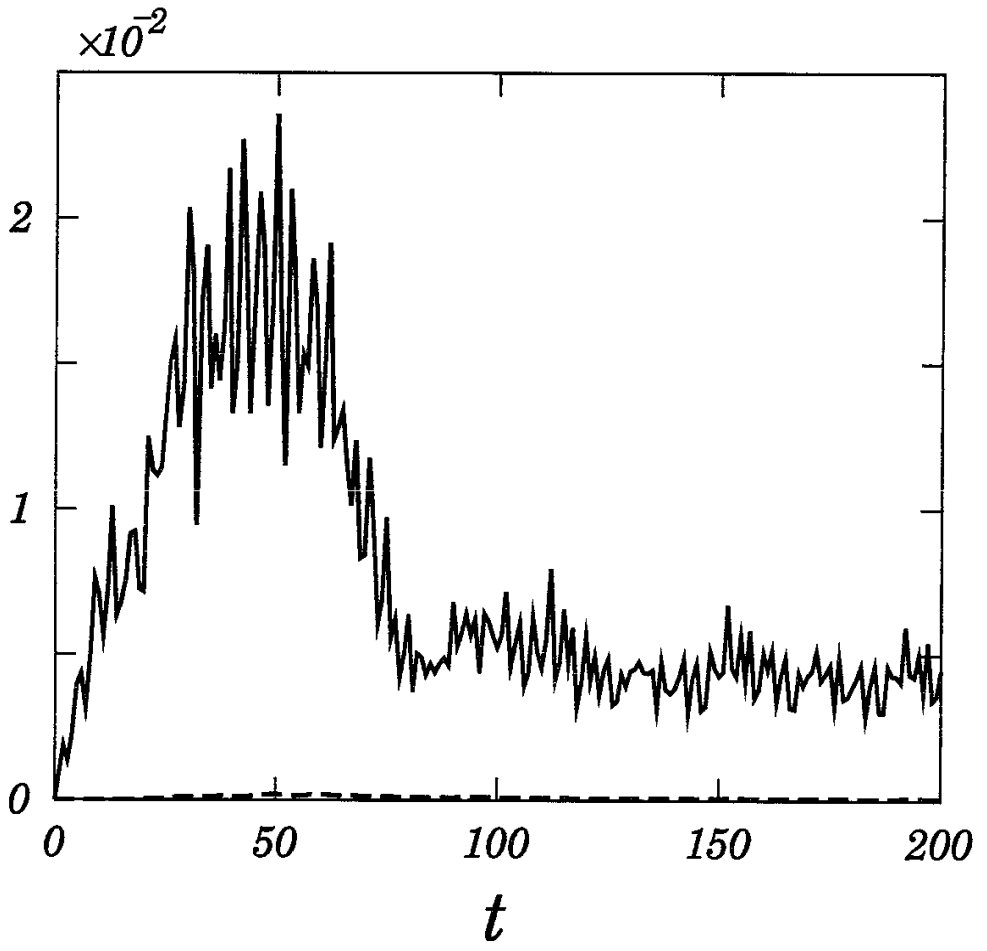

Figure 1 (a)

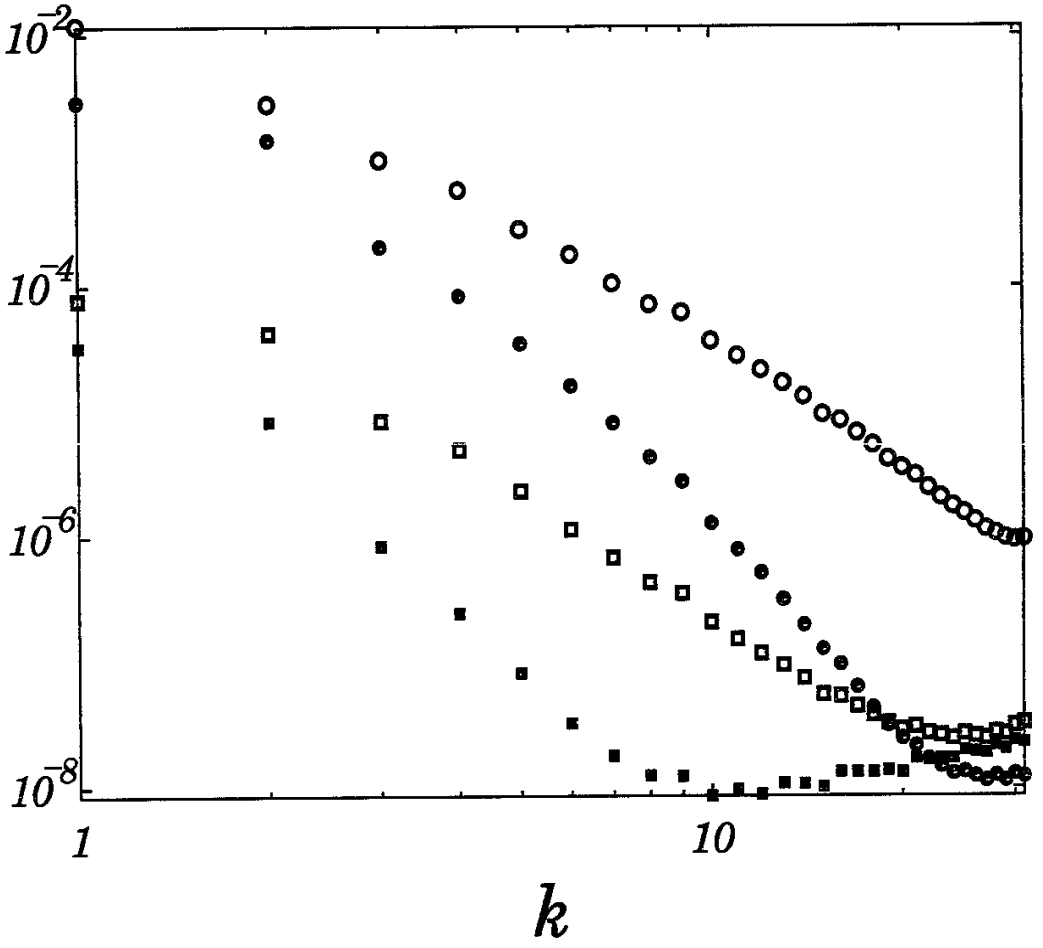

Figure 1 (b)

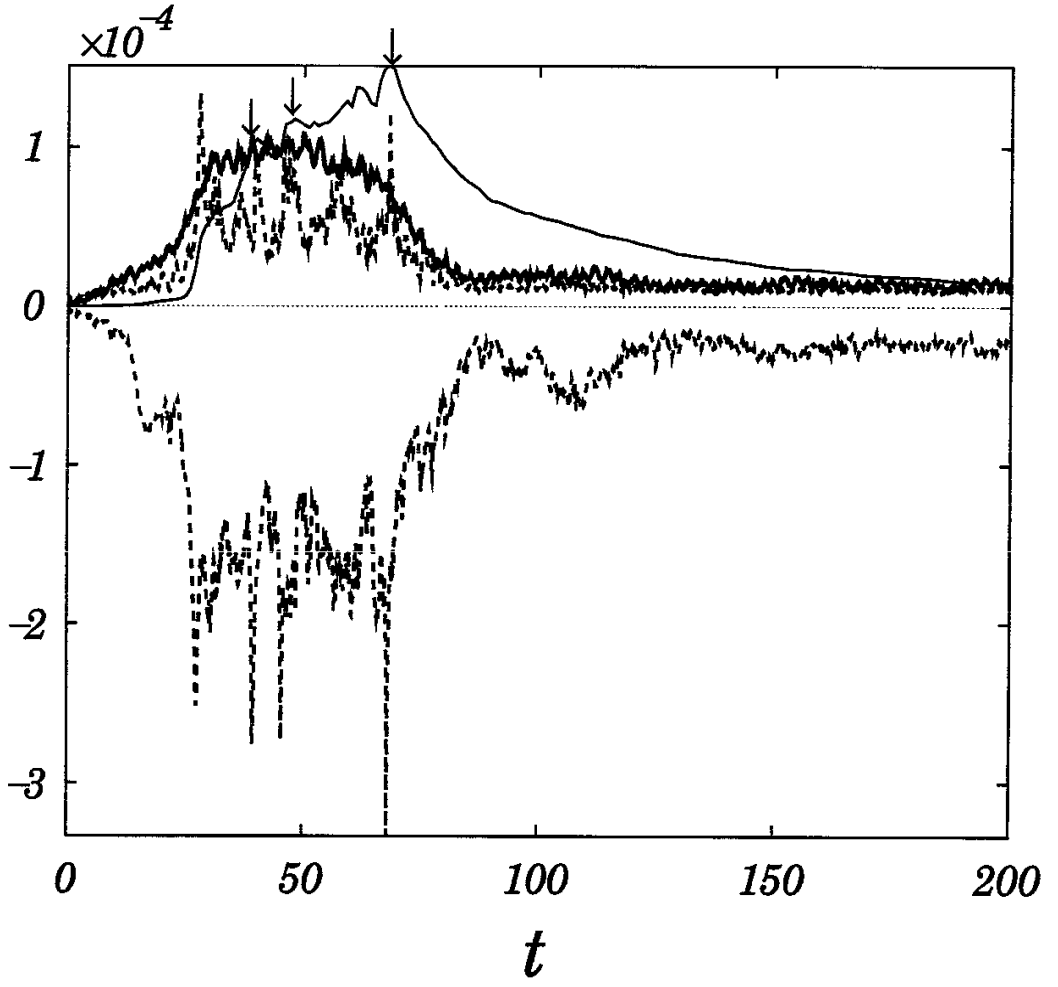

Figure 2 (a)

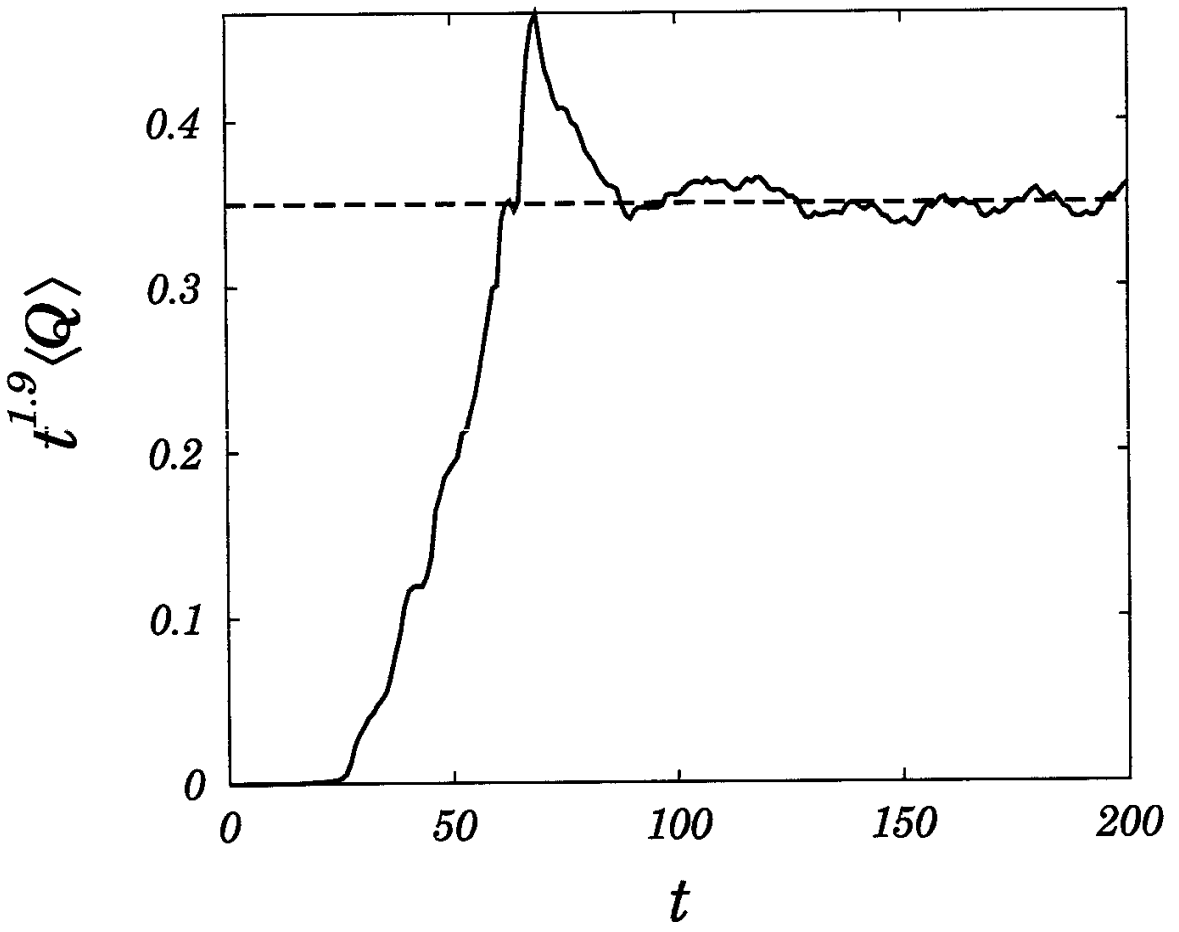

Figure 2 (b)

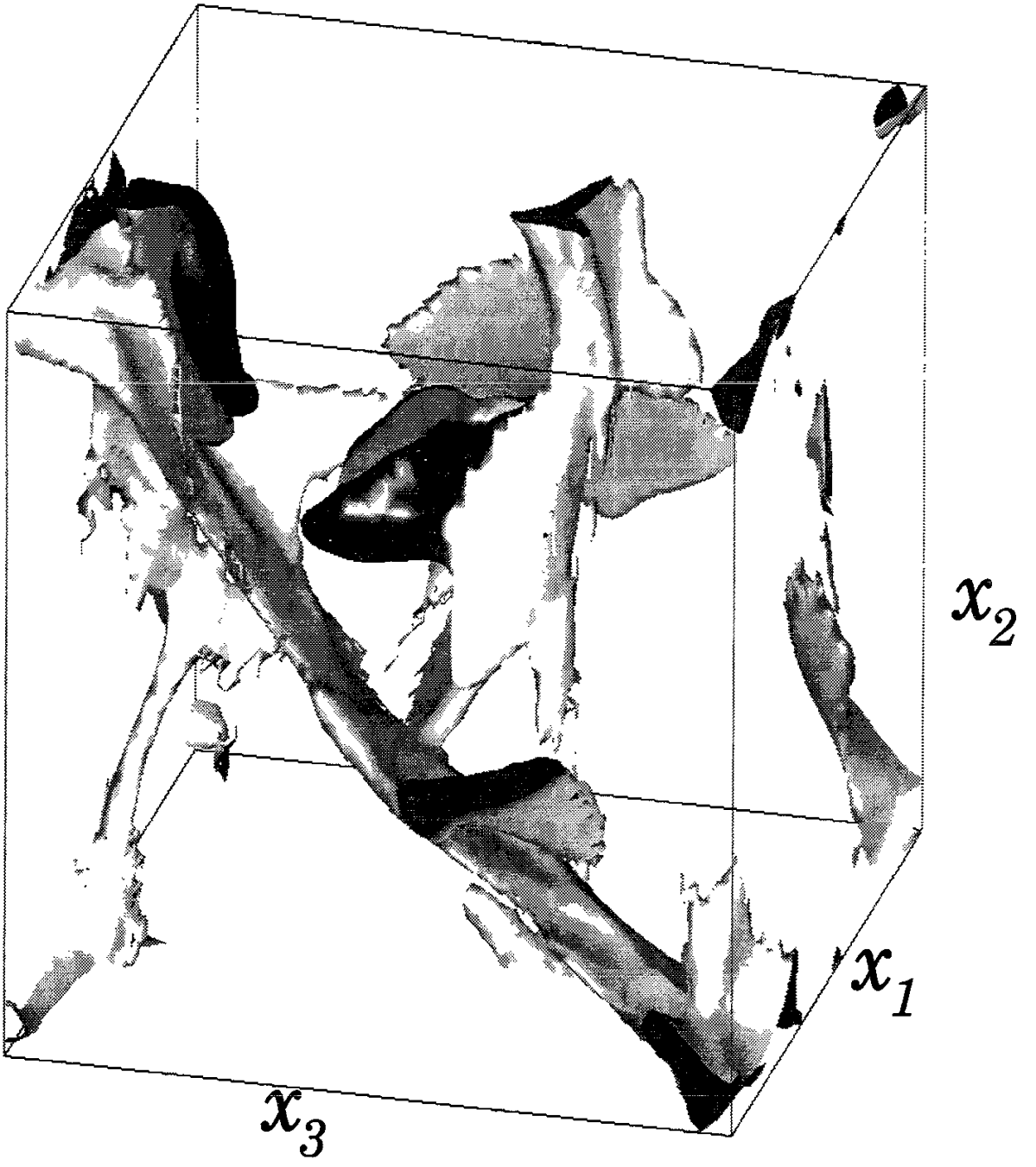

Figure 3

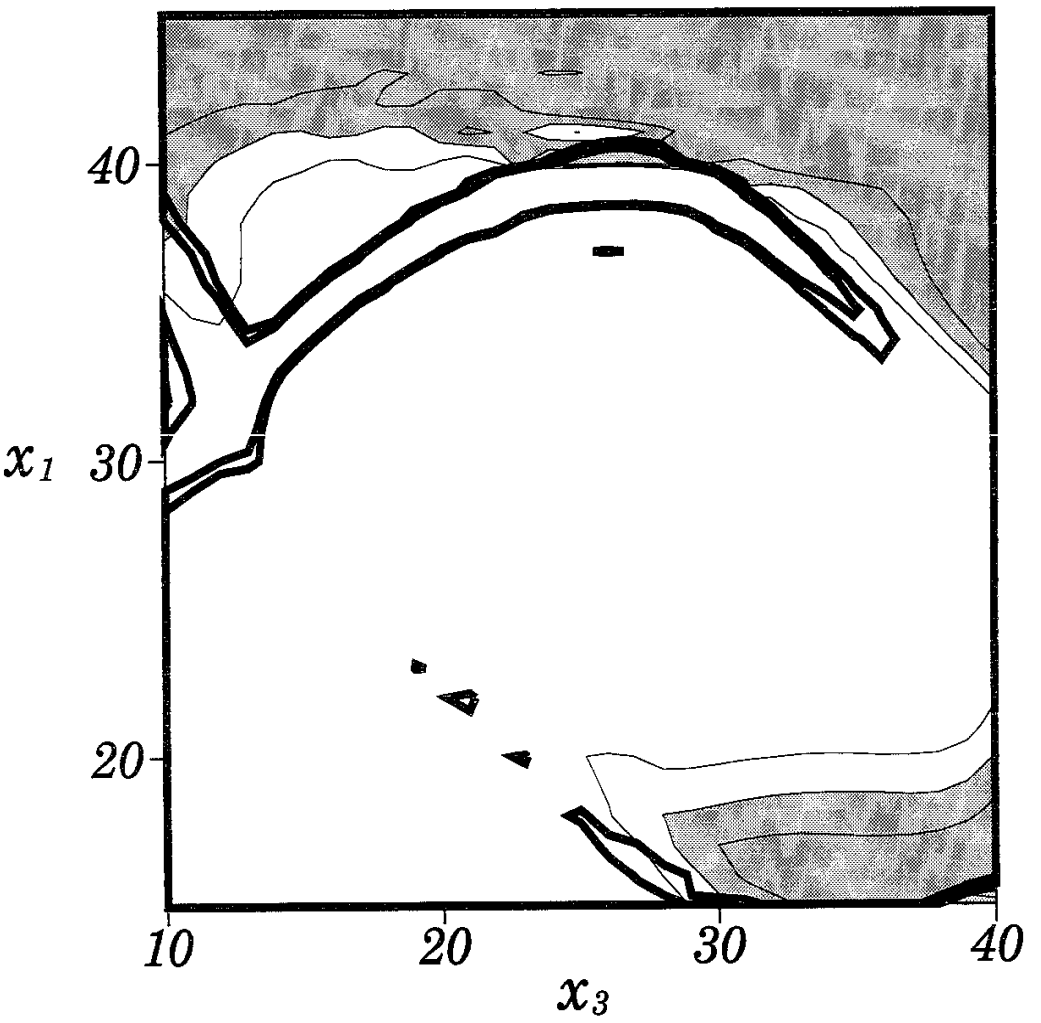

Figure 4

Figure 5

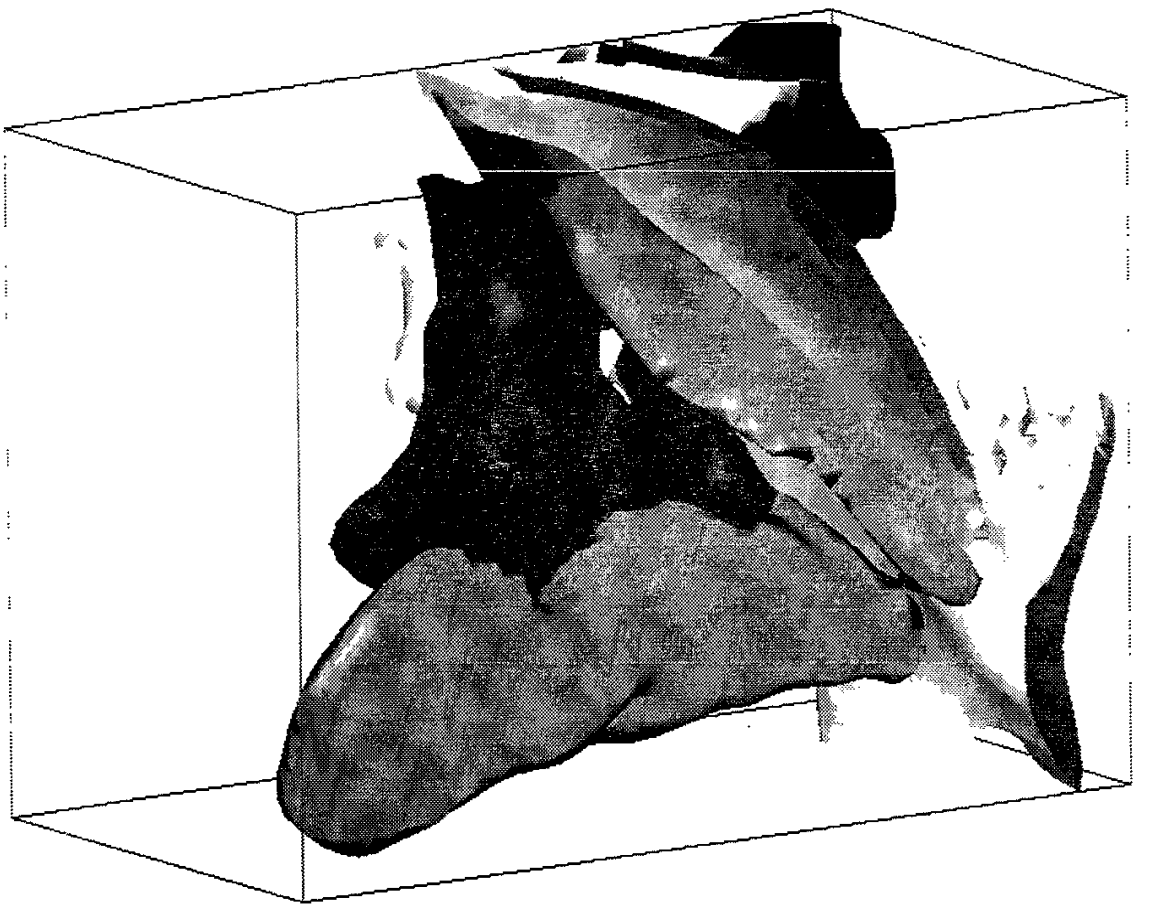

Figure 6 (a)

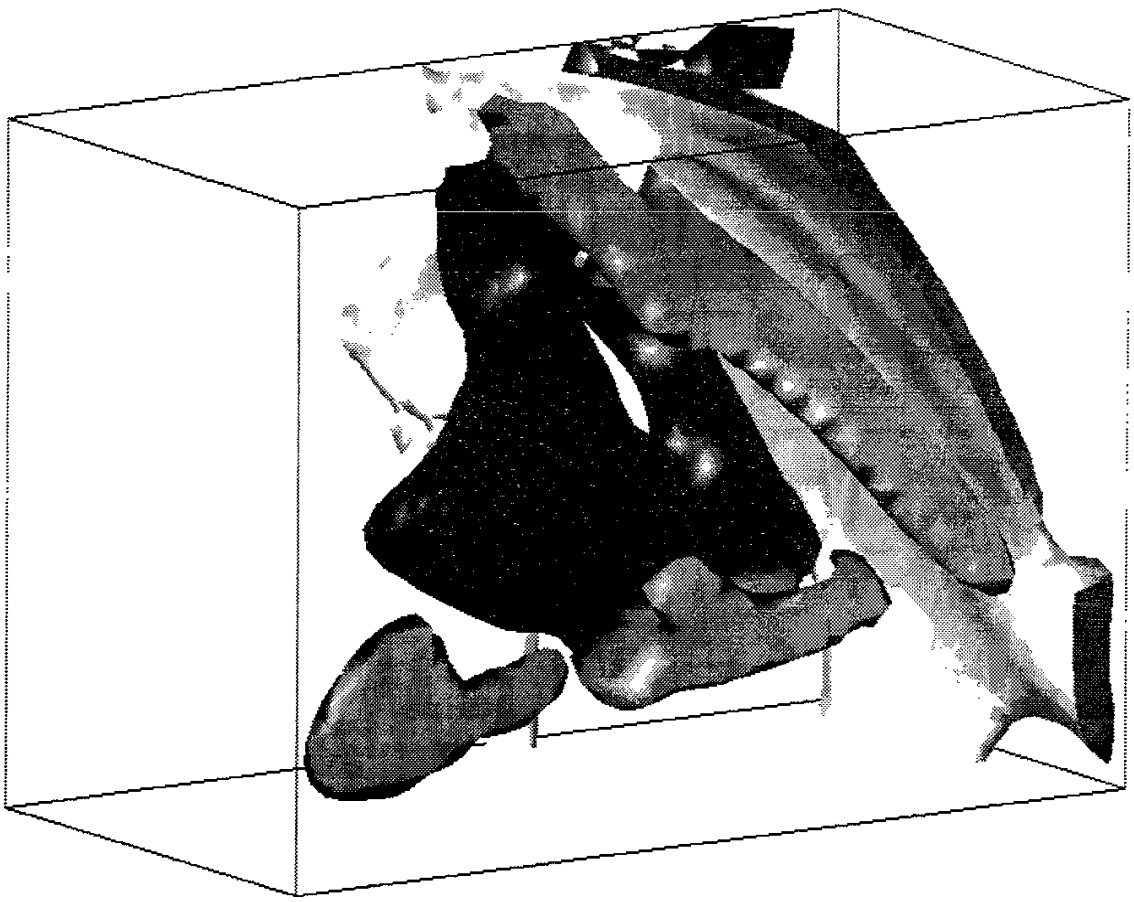

Figure 6 (b)

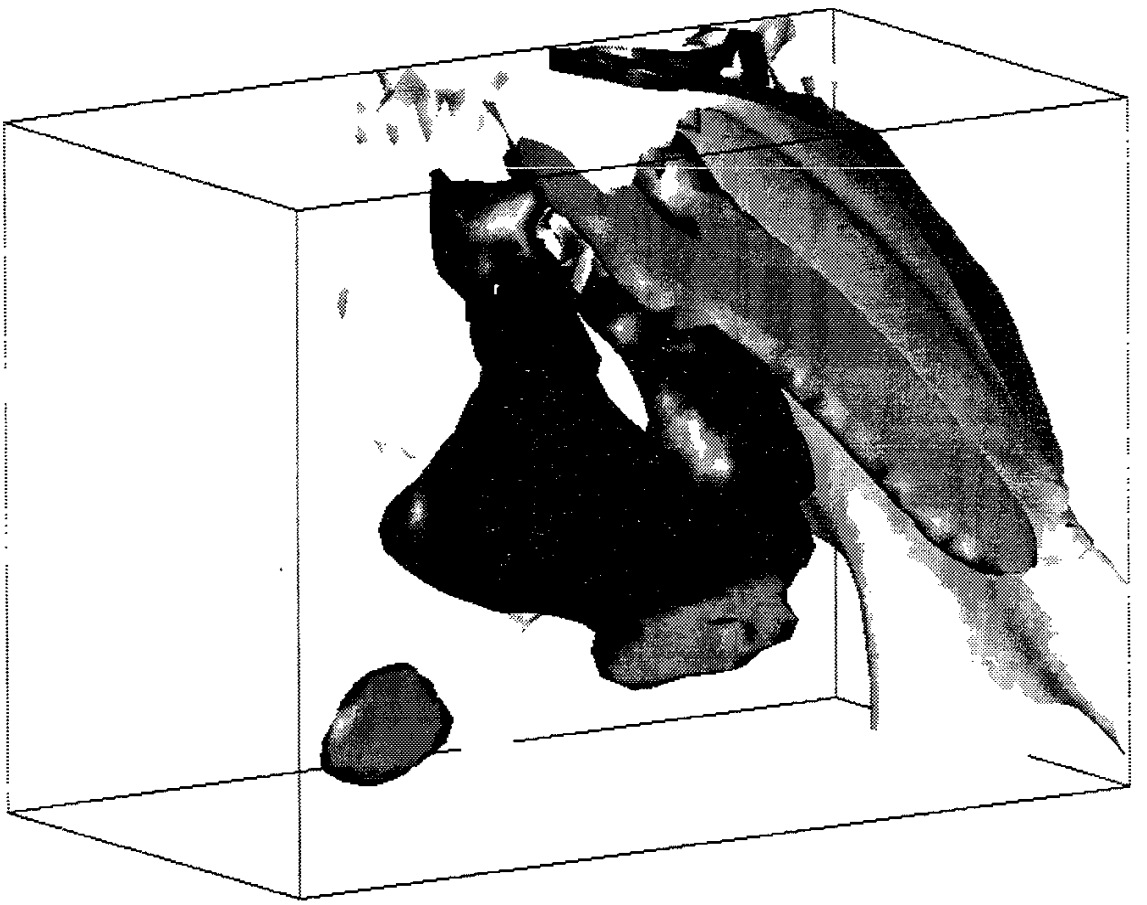

Figure 6 (c)

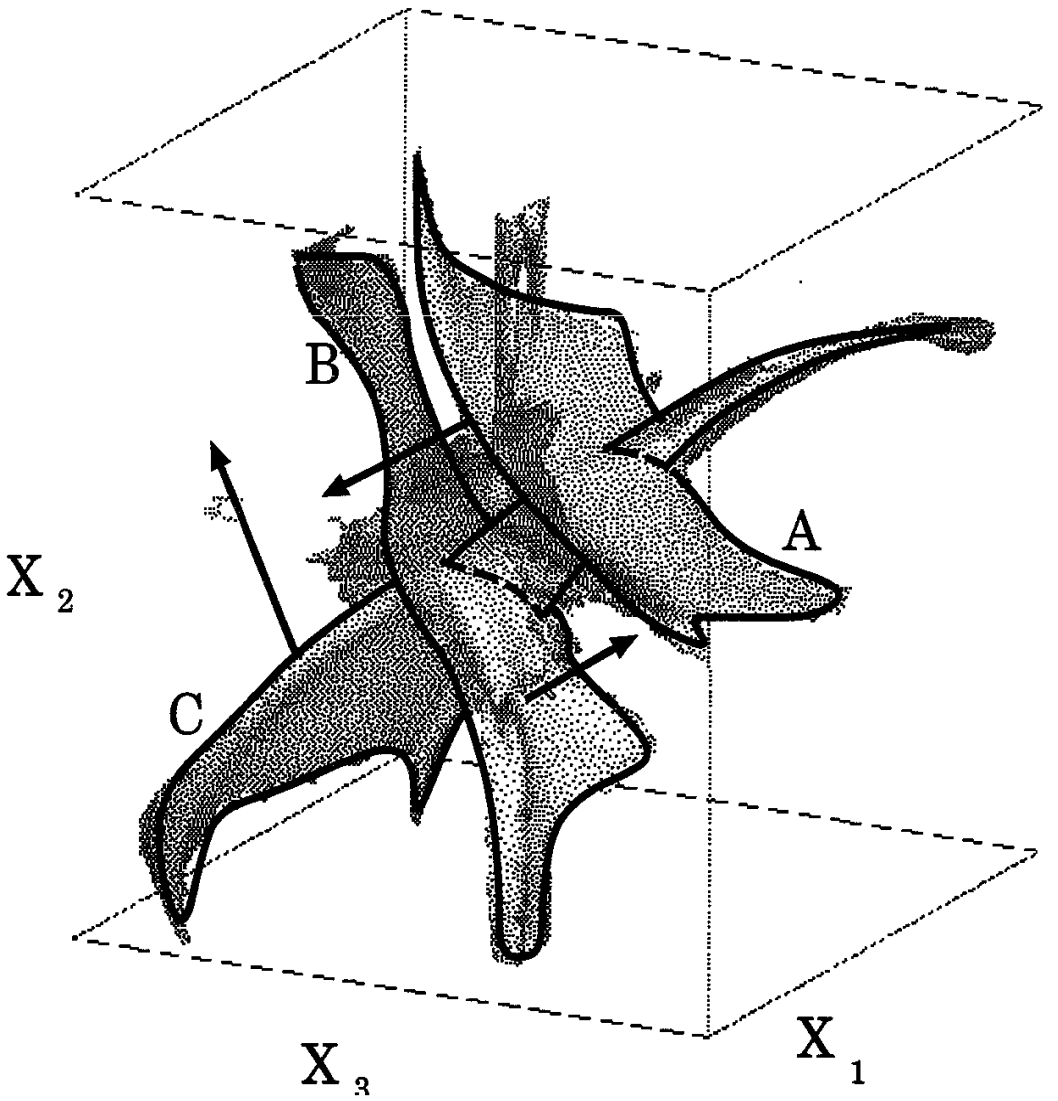

Figure 7 (a)

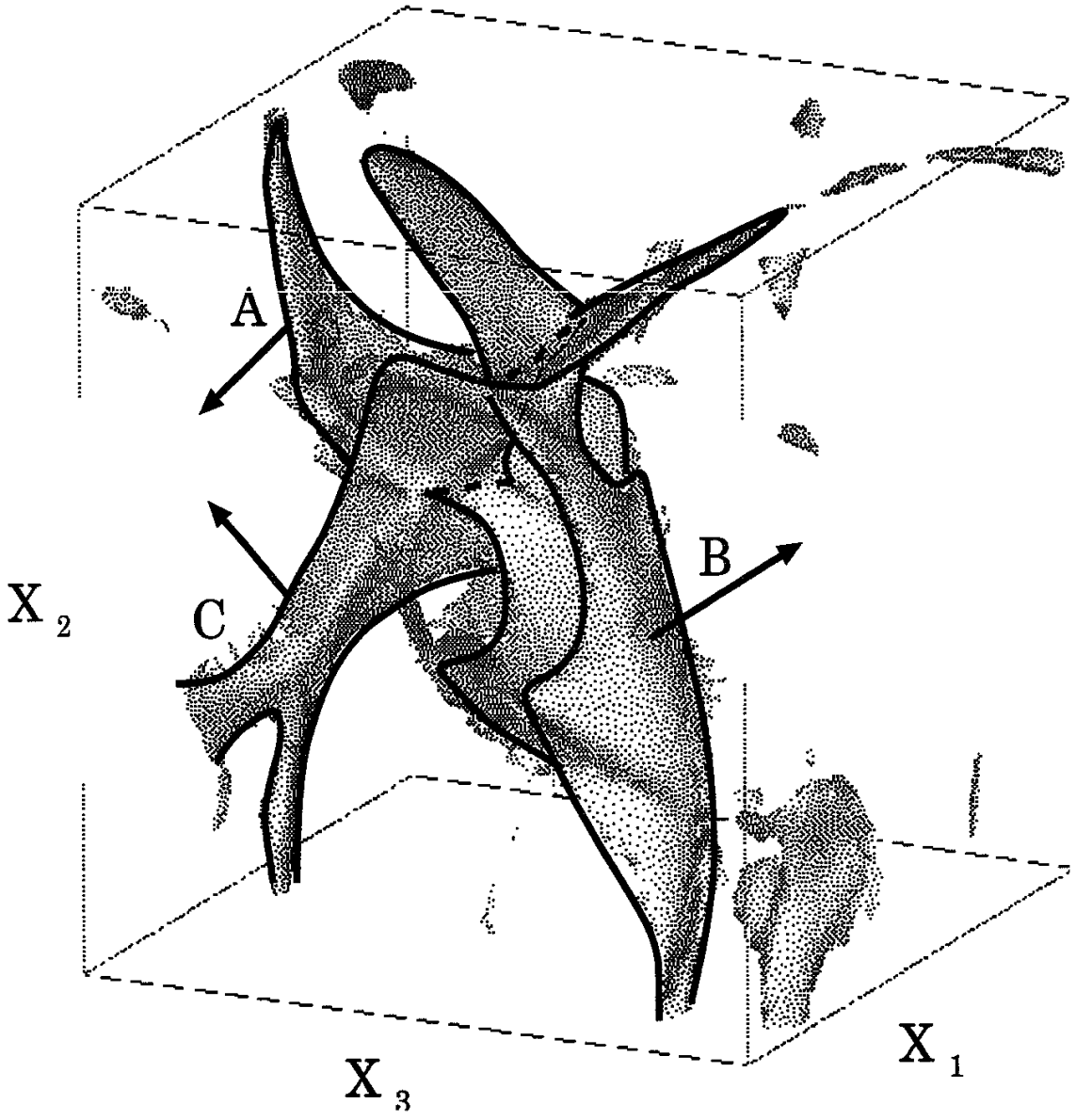

Figure 7 (b)

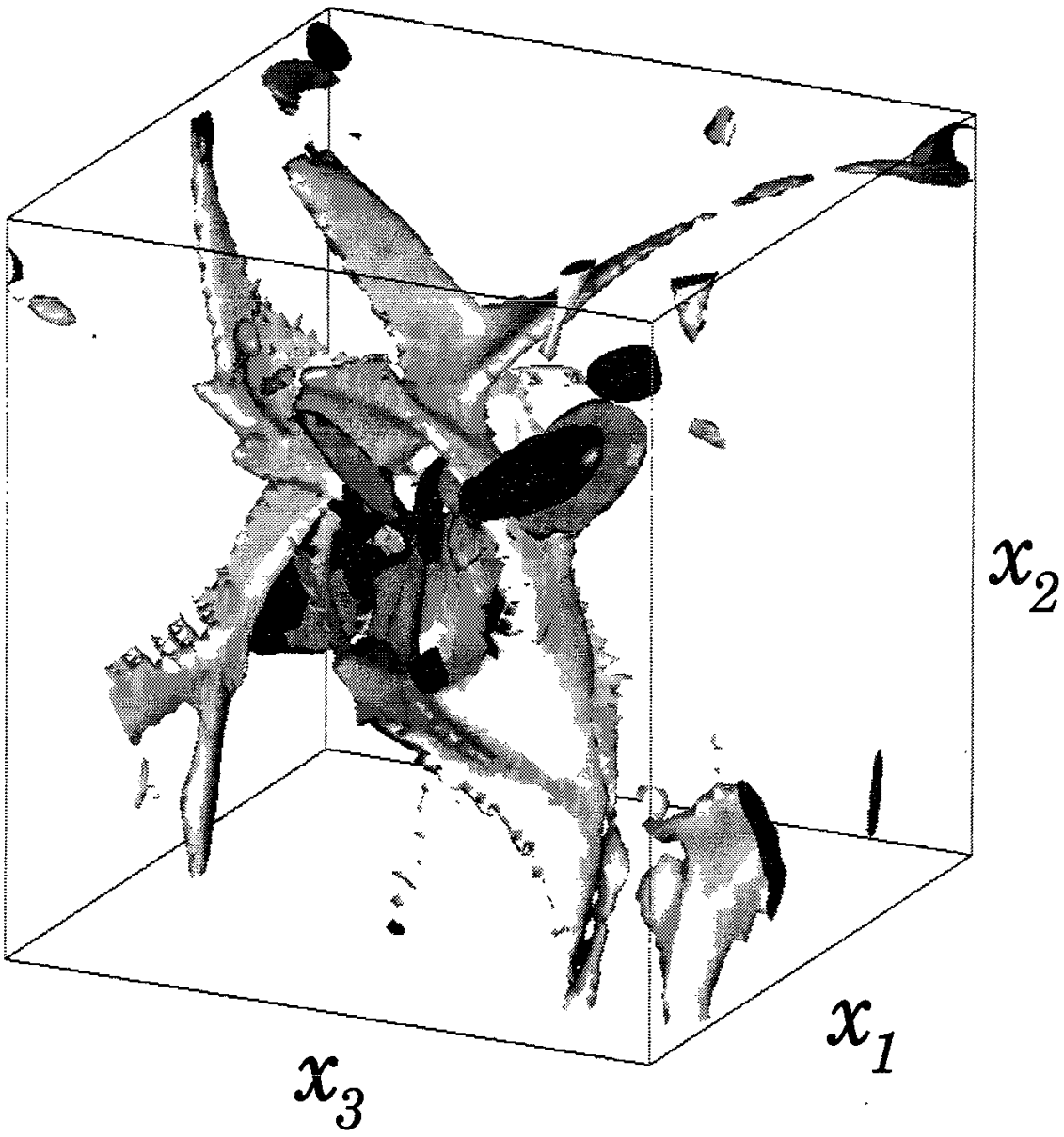

Figure 8 (a)

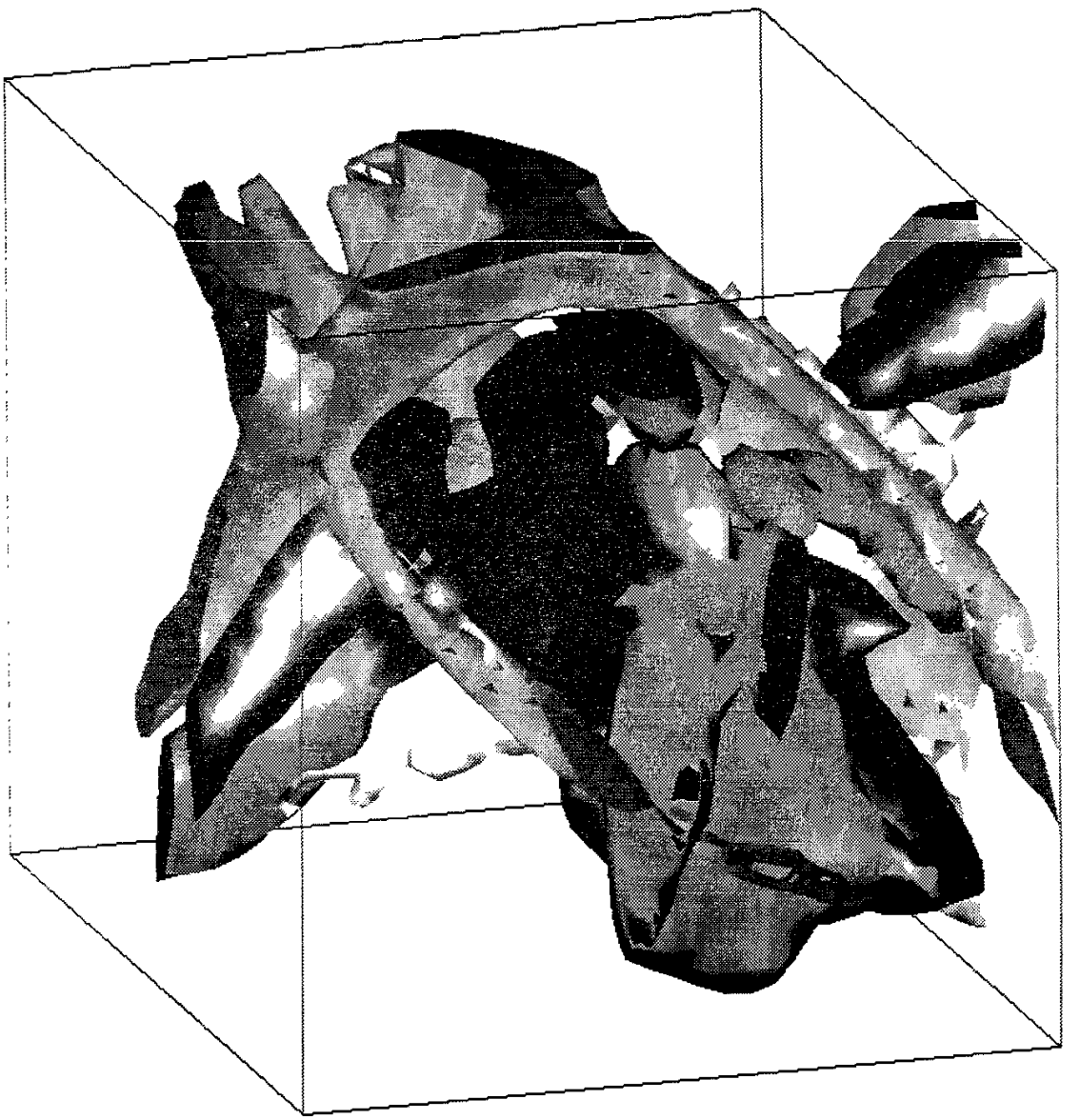

Figure 8 (b)

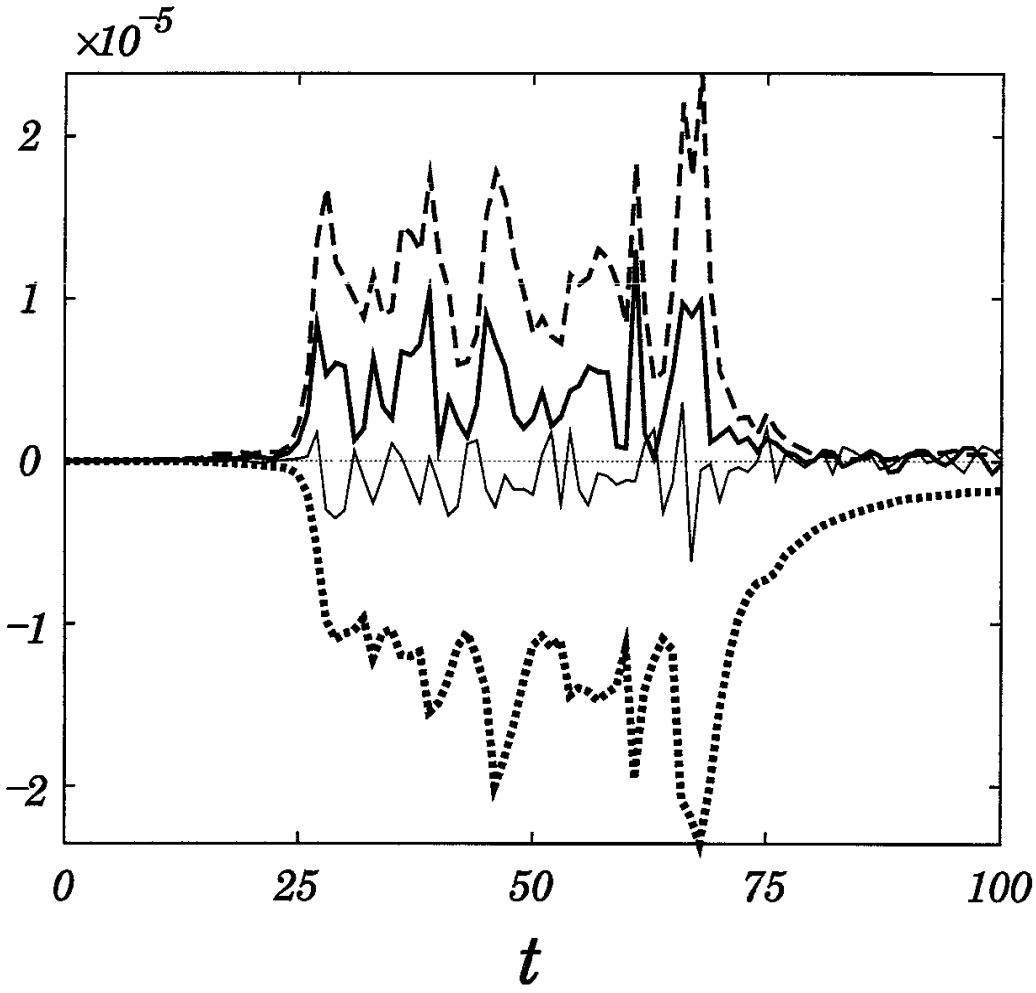

Figure 9

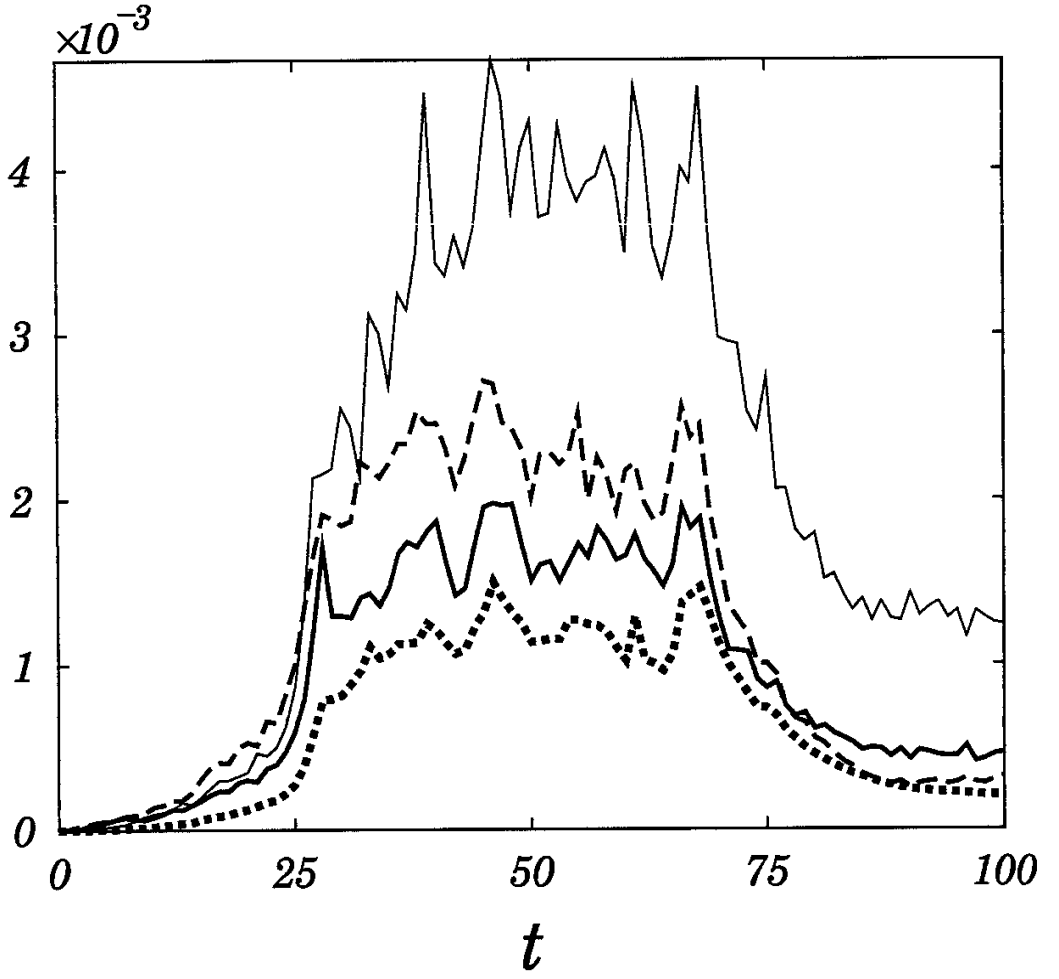

Figure 10

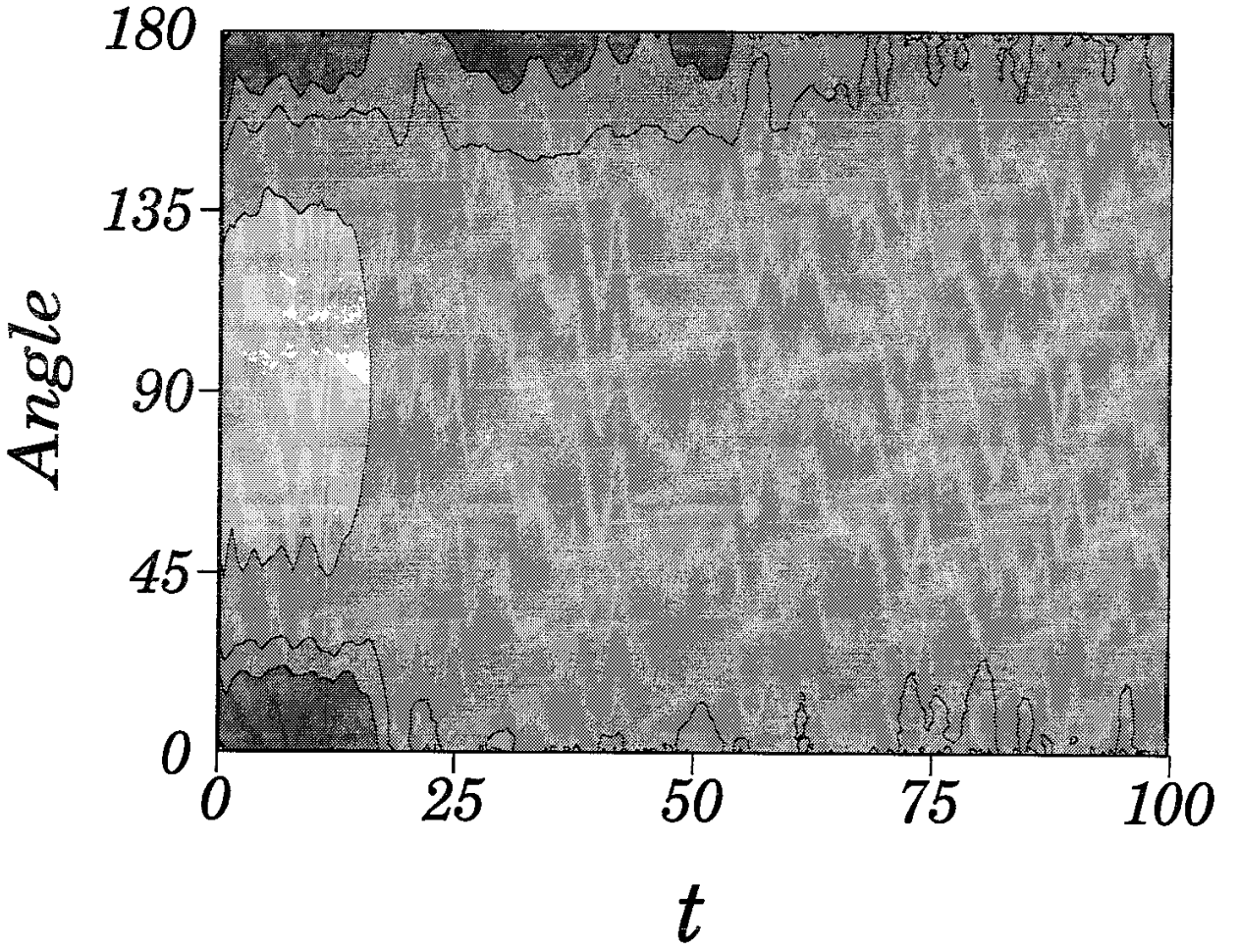

Figure 11 (a)

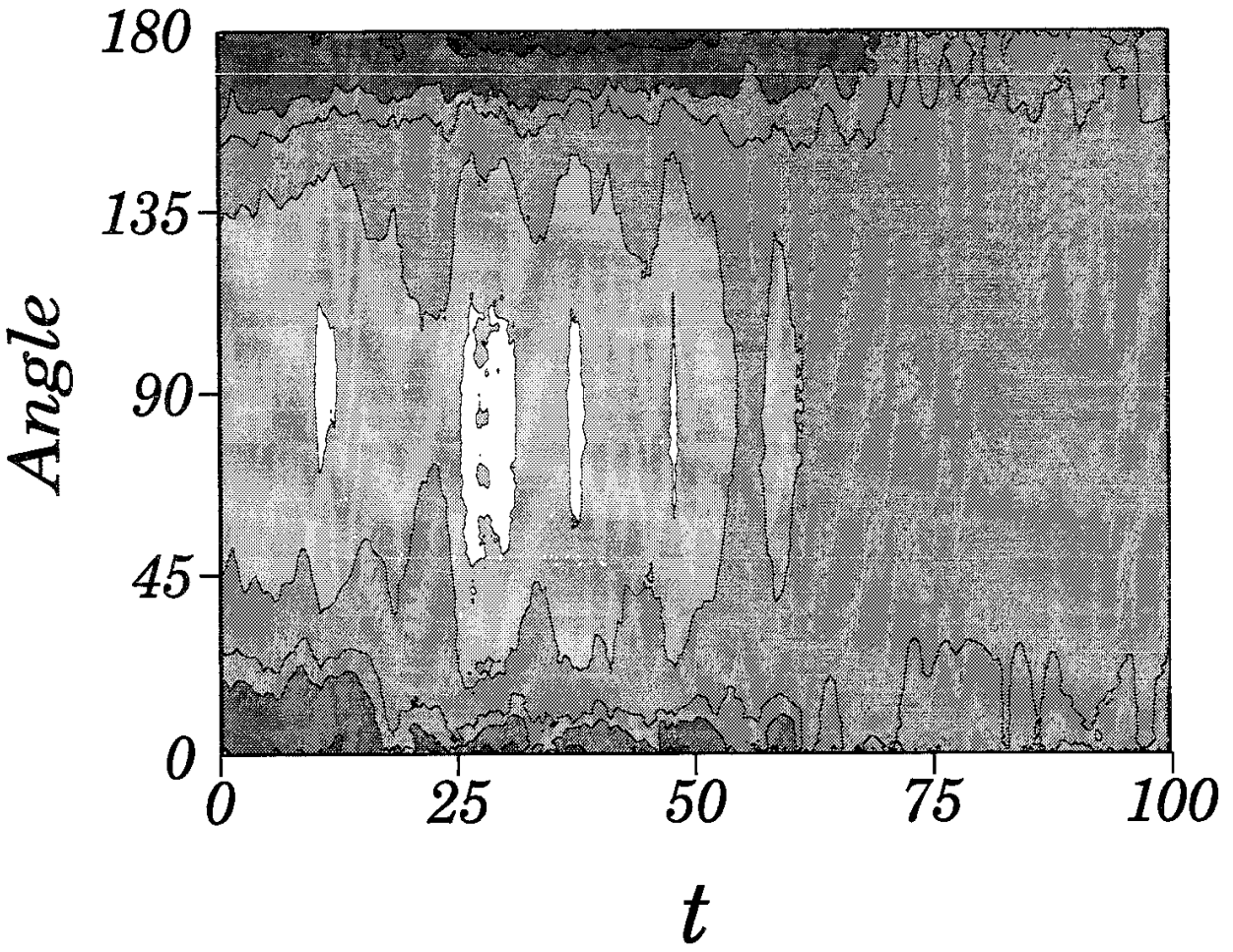

Figure 11 (b)

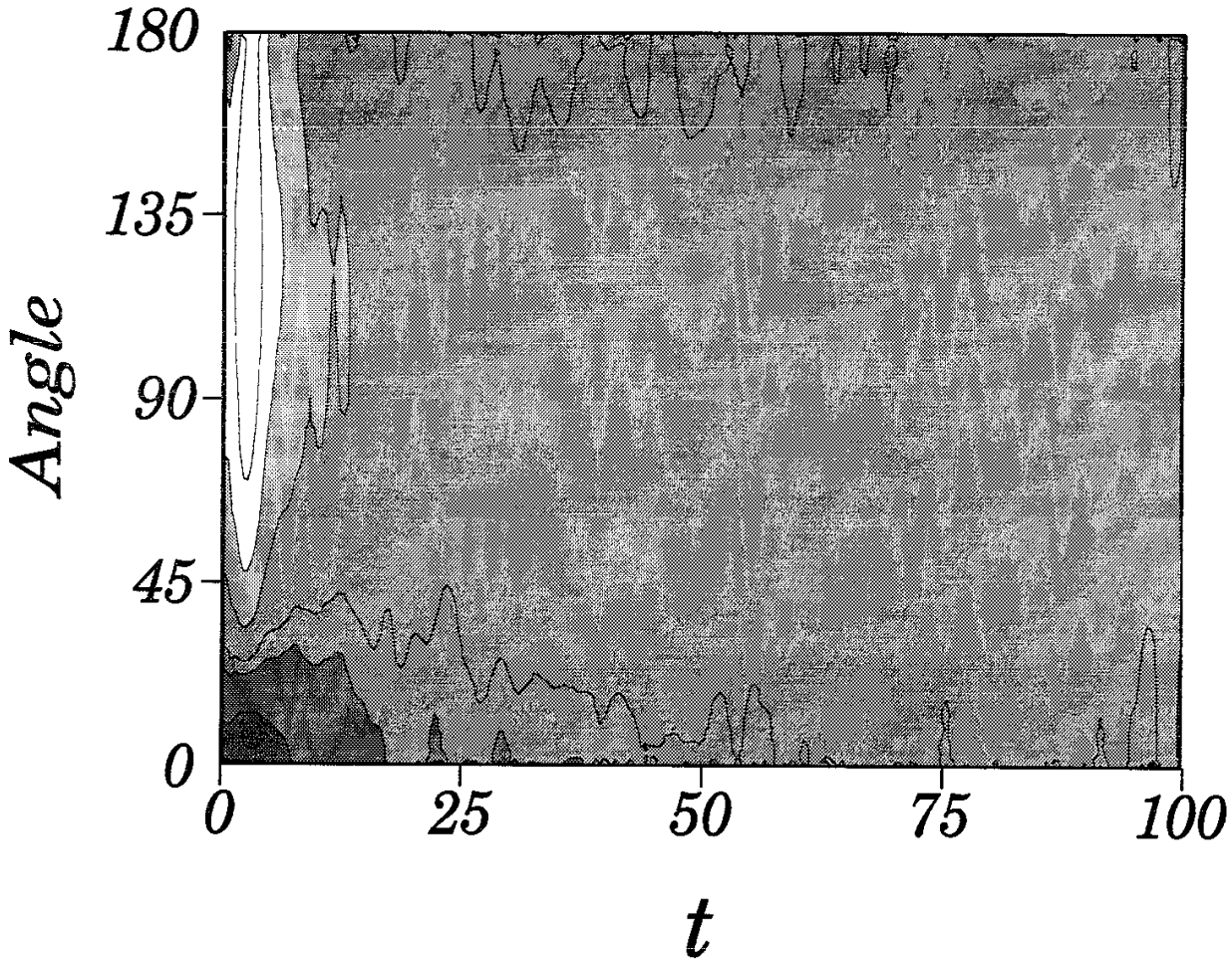

Figure 12 (a)

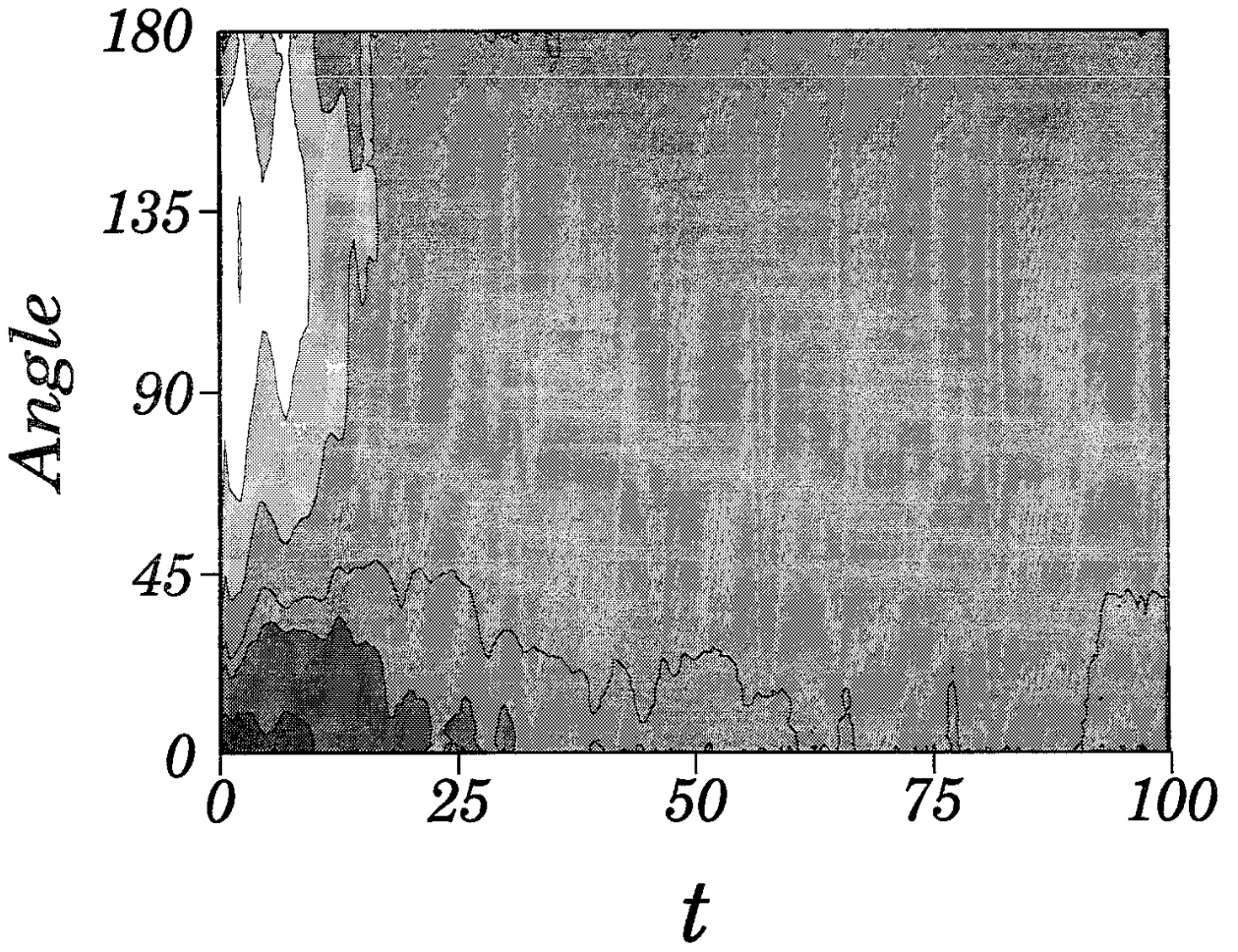

Figure 12 (b)

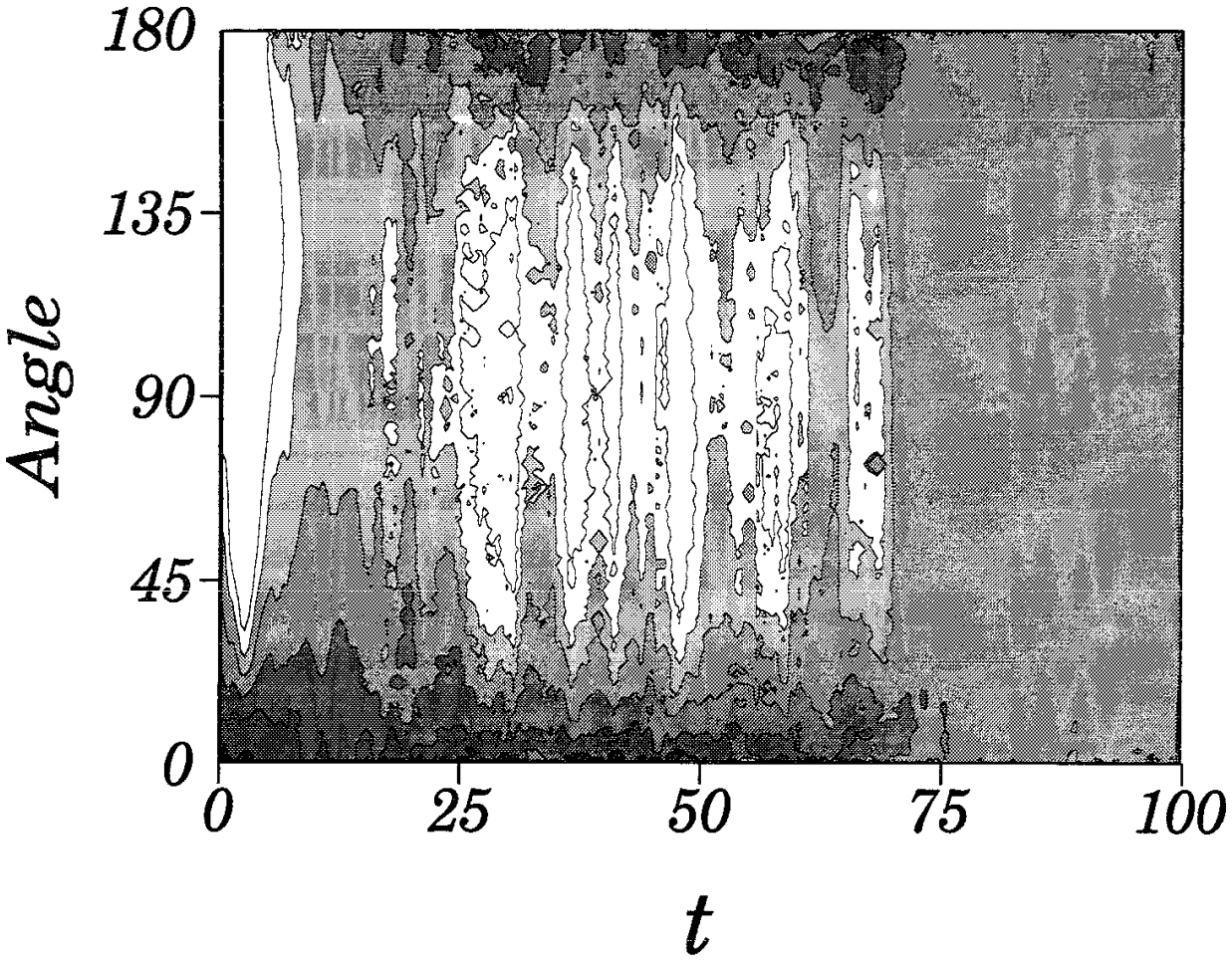

Figure 13 (a)

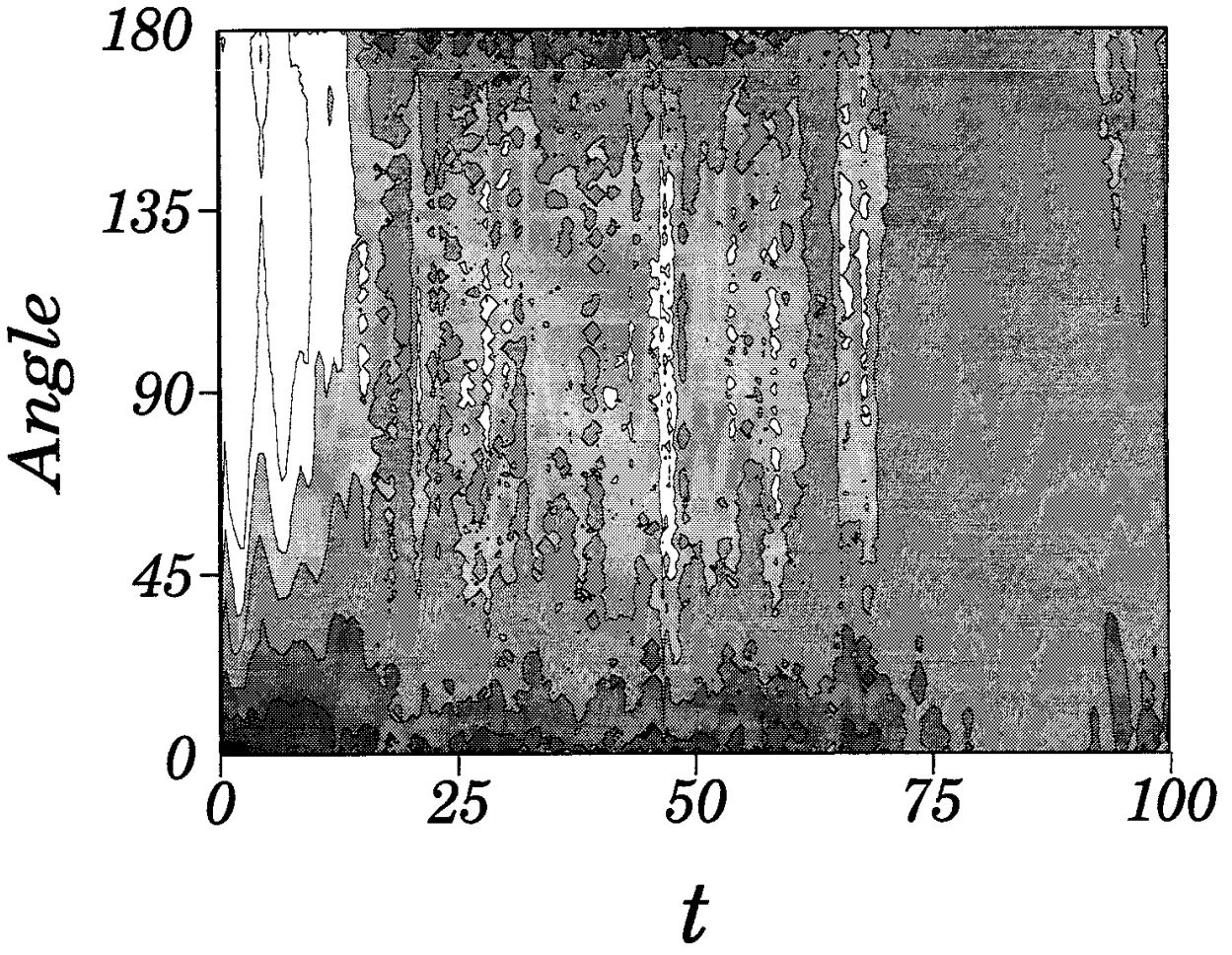

Figure 13 (b)

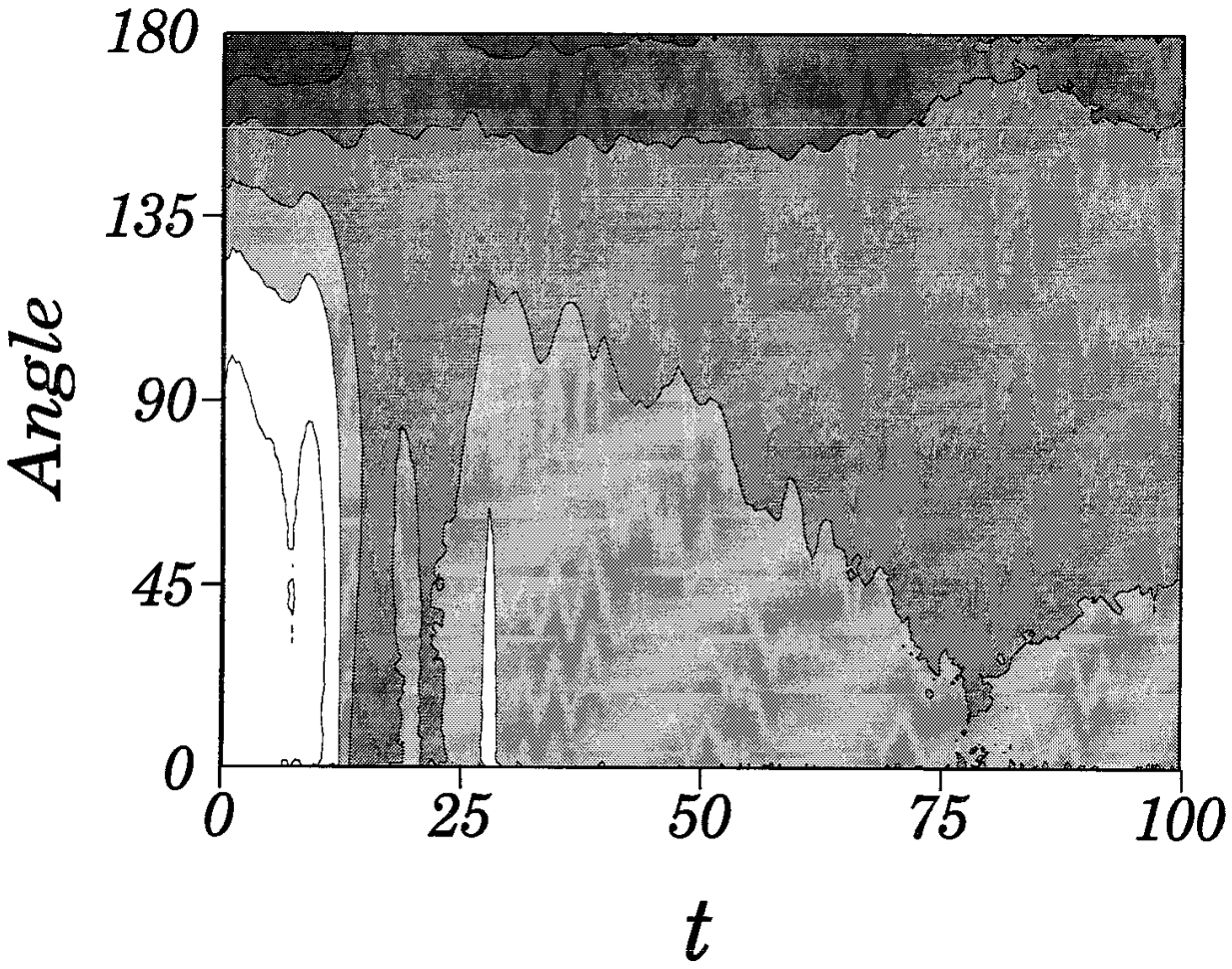

Figure 14 (a)

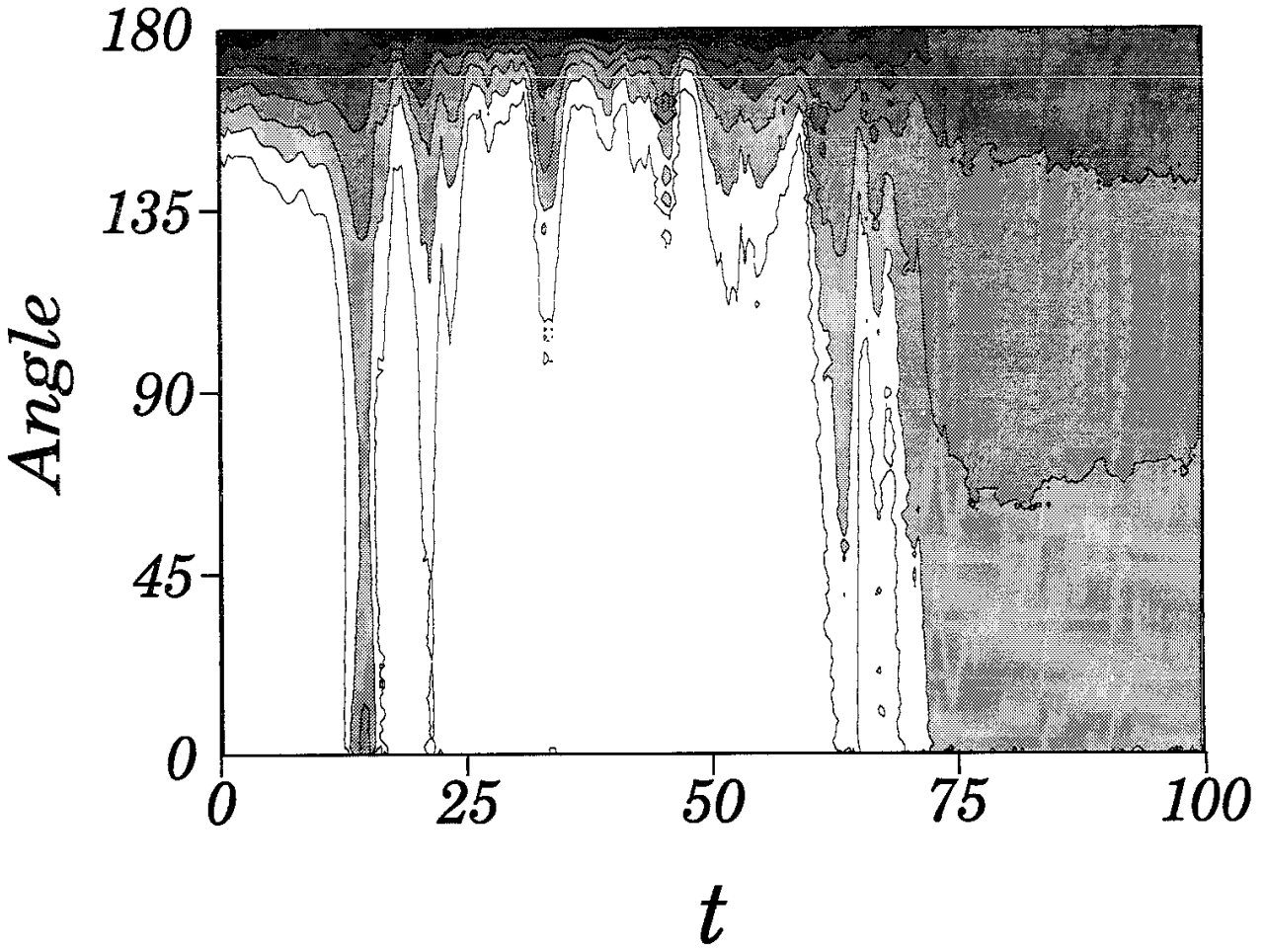

Figure 14 (b)

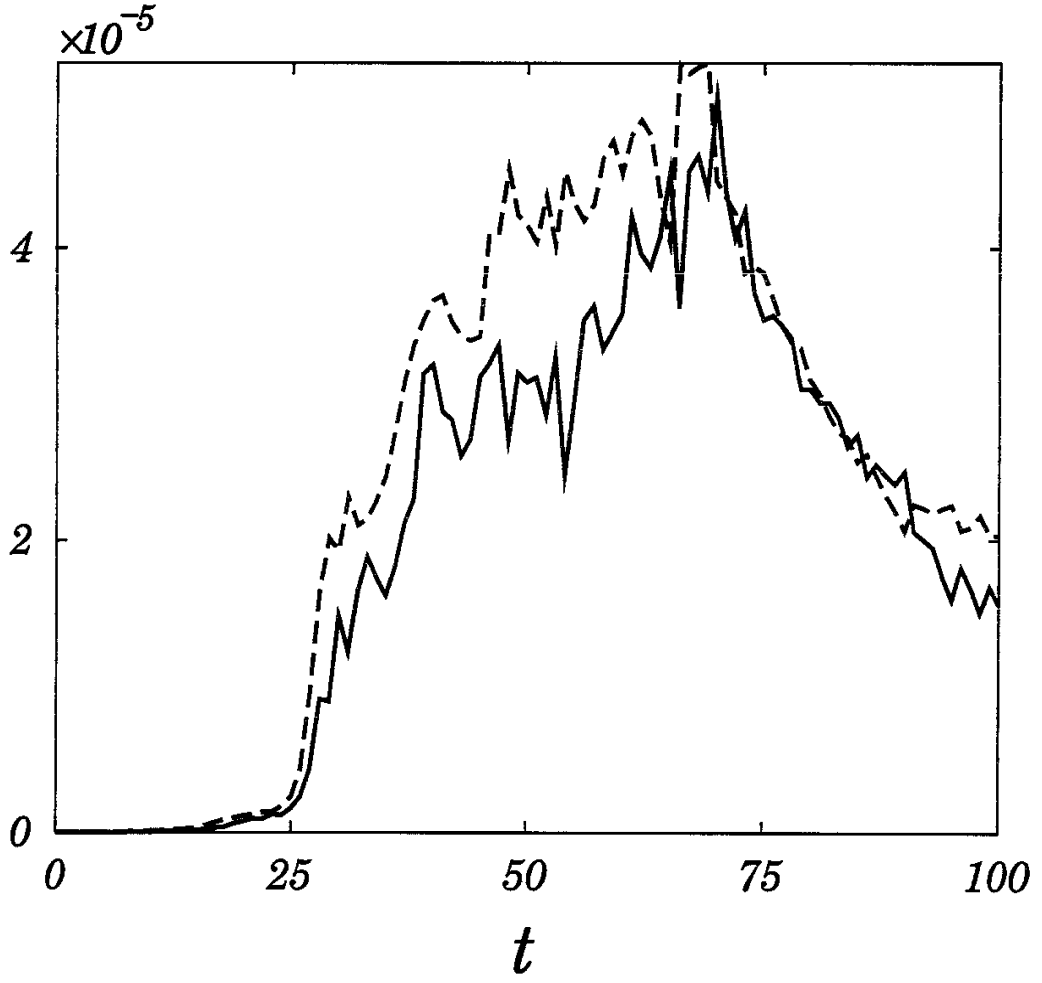

Figure 15 (a)

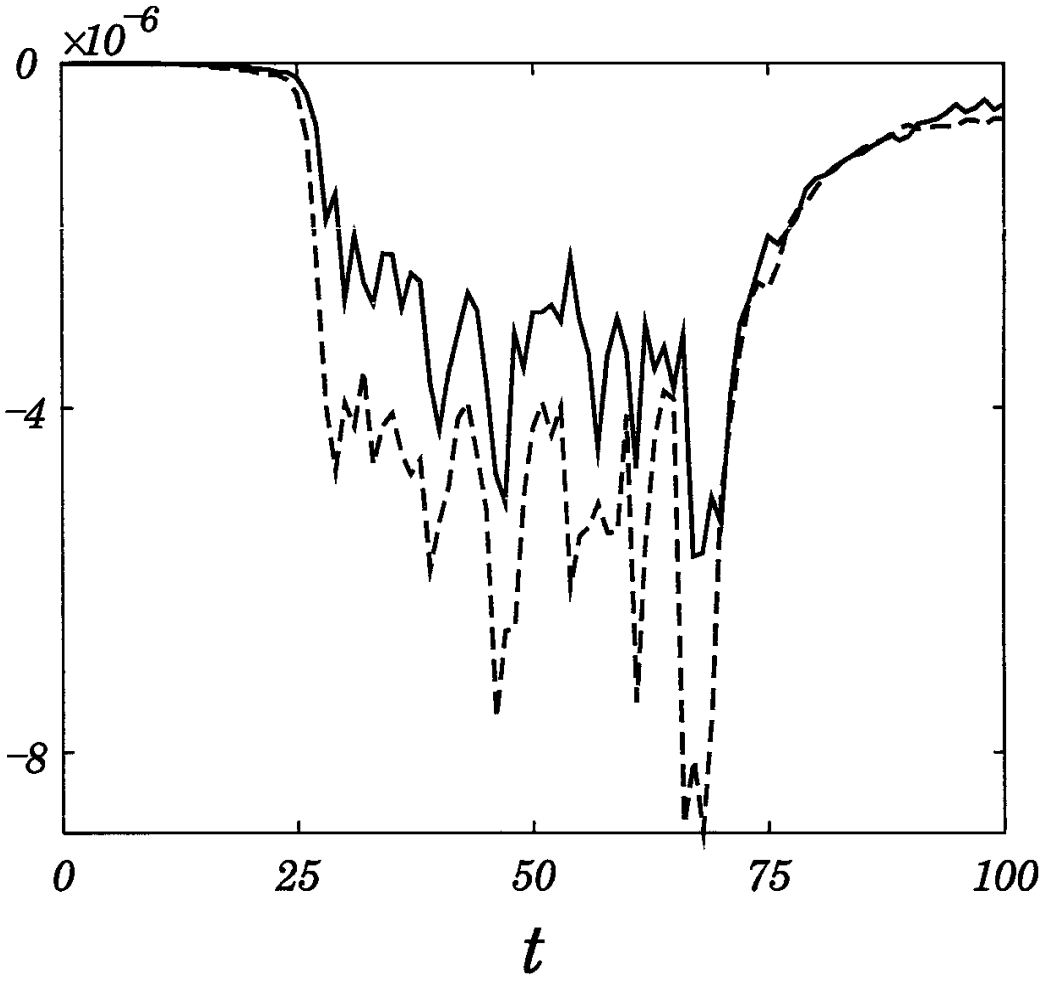

Figure 15 (b)

Recent Issues of NIFS Series

NIFS-324 V.D. Pustovitov
Quasisymmetry Equations for Conventional Stellarators; Nov. 1994

NIFS-325 A. Taniike, M. Sasao, Y. Hamada, J. Fujita, M. Wada,
The Energy Broadening Resulting from Electron Stripping Process of a Low Energy Au^- Beam; Dec. 1994

NIFS-326 I. Viniar and S. Sudo,
New Pellet Production and Acceleration Technologies for High Speed Pellet Injection System "HIPEL" in Large Helical Device; Dec. 1994

NIFS-327 Y. Hamada, A. Nishizawa, Y. Kawasumi, K. Kawahata, K. Itoh, A. Ejiri, K. Toi, K. Narihara, K. Sato, T. Seki, H. Iguchi, A. Fujisawa, K. Adachi, S. Hidekuma, S. Hirokura, K. Ida, M. Kojima, J. Koong, R. Kumazawa, H. Kuramoto, R. Liang, T. Minami, H. Sakakita, M. Sasao, K.N. Sato, T. Tsuzuki, J. Xu, I. Yamada, T. Watari,
Fast Potential Change in Sawteeth in JIPP T-IIU Tokamak Plasmas; Dec. 1994

NIFS-328 V.D. Pustovitov,
Effect of Satellite Helical Harmonics on the Stellarator Configuration; Dec. 1994

NIFS-329 K. Itoh, S-I. Itoh and A. Fukuyama,
A Model of Sawtooth Based on the Transport Catastrophe; Dec. 1994

NIFS-330 K. Nagasaki, A. Ejiri,
Launching Conditions for Electron Cyclotron Heating in a Sheared Magnetic Field; Jan. 1995

NIFS-331 T.H. Watanabe, Y. Todo, R. Horiuchi, K. Watanabe, T. Sato,
An Advanced Electrostatic Particle Simulation Algorithm for Implicit Time Integration; Jan. 1995

NIFS-332 N. Bekki and T. Karakisawa,
Bifurcations from Periodic Solution in a Simplified Model of Two-dimensional Magnetoconvection; Jan. 1995

NIFS-333 K. Itoh, S.-I. Itoh, M. Yagi, A. Fukuyama,
Theory of Anomalous Transport in Reverse Field Pinch; Jan. 1995

NIFS-334 K. Nagasaki, A. Isayama and A. Ejiri
Application of Grating Polarizer to 106.4GHz ECH System on Heliotron-E; Jan. 1995

NIFS-335 H. Takamaru, T. Sato, R. Horiuchi, K. Watanabe and Complexity Simulation

Group,
A Self-Consistent Open Boundary Model for Particle Simulation in Plasmas; Feb. 1995

NIFS-336 B.B. Kadomtsev,
Quantum Telegragh : is it possible?; Feb. 1995

NIFS-337 B.B.Kadomtsev,
Ball Lightning as Self-Organization Phenomenon; Feb. 1995

NIFS-338 Y. Takeiri, A. Ando, O. Kaneko, Y. Oka, K. Tsumori, R. Akiyama, E. Asano, T. Kawamoto, M. Tanaka and T. Kuroda,
High-Energy Acceleration of an Intense Negative Ion Beam; Feb. 1995

NIFS-339 K. Toi, T. Morisaki, S. Sakakibara, S. Ohdachi, T.Minami, S. Morita, H. Yamada, K. Tanaka, K. Ida, S. Okamura, A. Ejiri, H. Iguchi, K. Nishimura, K. Matsuoka, A. Ando, J. Xu, I. Yamada, K. Narihara, R. Akiyama, H. Idei, S. Kubo, T. Ozaki, C. Takahashi, K. Tsumori,
H-Mode Study in CHS; Feb. 1995

NIFS-340 T. Okada and H. Tazawa,
Filamentation Instability in a Light Ion Beam-plasma System with External Magnetic Field; Feb. 1995

NIFS-341 T. Watanbe, G. Gnudi,
A New Algorithm for Differential-Algebraic Equations Based on HIDM; Feb. 13, 1995

NIFS-342 Y. Nejoh,
New Stationary Solutions of the Nonlinear Drift Wave Equation; Feb. 1995

NIFS-343 A. Ejiri, S. Sakakibara and K. Kawahata,
Signal Based Mixing Analysis for the Magnetohydrodynamic Mode Reconstruction from Homodyne Microwave Reflectometry; Mar.. 1995

NIFS-344 B.B.Kadomtsev, K. Itoh, S.-I. Itoh
Fast Change in Core Transport after L-H Transition; Mar. 1995

NIFS-345 W.X. Wang, M. Okamoto, N. Nakajima and S. Murakami,
An Accurate Nonlinear Monte Carlo Collision Operator; Mar. 1995

NIFS-346 S. Sasaki, S. Takamura, S. Masuzaki, S. Watanabe, T. Kato, K. Kadota,
Helium I Line Intensity Ratios in a Plasma for the Diagnostics of Fusion Edge Plasmas; Mar. 1995

NIFS-347 M. Osakabe,
Measurement of Neutron Energy on D-T Fusion Plasma Experiments; Apr. 1995

NIFS-348 M. Sita Janaki, M.R. Gupta and Brahmananda Dasgupta,
Adiabatic Electron Acceleration in a Cnoidal Wave; Apr. 1995

NIFS-349 J. Xu, K. Ida and J. Fujita,
A Note for Pitch Angle Measurement of Magnetic Field in a Toroidal Plasma Using Motional Stark Effect; Apr. 1995

NIFS-350 J. Uramoto,
Characteristics for Metal Plate Penetration of a Low Energy Negative Muonlike or Pionlike Particle Beam: Apr. 1995

NIFS-351 J. Uramoto,
An Estimation of Life Time for A Low Energy Negative Pionlike Particle Beam: Apr. 1995

NIFS-352 A. Taniike,
Energy Loss Mechanism of a Gold Ion Beam on a Tandem Acceleration System: May 1995

NIFS-353 A. Nishizawa, Y. Hamada, Y. Kawasumi and H. Iguchi,
Increase of Lifetime of Thallium Zeolite Ion Source for Single-Ended Accelerator: May 1995

NIFS-354 S. Murakami, N. Nakajima, S. Okamura and M. Okamoto,
Orbital Aspects of Reachable β Value in NBI Heated Heliotron/Torsatrons; May 1995

NIFS-355 H. Sugama and W. Horton,
Neoclassical and Anomalous Transport in Axisymmetric Toroidal Plasmas with Electrostatic Turbulence; May 1995

NIFS-356 N. Ohyabu
A New Boundary Control Scheme for Simultaneous Achievement of H-mode and Radiative Cooling (SHC Boundary); May 1995

NIFS-357 Y. Hamada, K.N. Sato, H. Sakakita, A. Nishizawa, Y. Kawasumi, R. Liang, K. Kawahata, A. Ejiri, K. Toi, K. Narihara, K. Sato, T. Seki, H. Iguchi, A. Fujisawa, K. Adachi, S. Hidekuma, S. Hirokura, K. Ida, M. Kojima, J. Koong, R. Kumazawa, H. Kuramoto, T. Minami,. M. Sasao, T. Tsuzuki, J.Xu, I. Yamada, and T. Watari,
Large Potential Change Induced by Pellet Injection in JIPP T-IIU Tokamak Plasmas; May 1995

NIFS-358 M. Ida and T. Yabe,
Implicit CIP (Cubic-Interpolated Propagation) Method in One Dimension; May 1995

NIFS-359 A. Kageyama, T. Sato and The Complexity Simulation Group,

Computer Has Solved A Historical Puzzle: Generation of Earth's Dipole Field; June 1995

NIFS-360 K. Itoh, S.-I. Itoh, M. Yagi and A. Fukuyama,
Dynamic Structure in Self-Sustained Turbulence; June 1995

NIFS-361 K. Kamada, H. Kinoshita and H. Takahashi,
Anomalous Heat Evolution of Deuteron Implanted Al on Electron Bombardment; June 1995

NIFS-362 V.D. Pustovitov,
Suppression of Pfirsch-schlüter Current by Vertical Magnetic Field in Stellarators; June 1995

NIFS-363 A. Ida, H. Sanuki and J. Todoroki
An Extended K-dV Equation for Nonlinear Magnetosonic Wave in a Multi-Ion Plasma; June 1995

NIFS-364 H. Sugama and W. Horton
Entropy Production and Onsager Symmetry in Neoclassical Transport Processes of Toroidal Plasmas; July 1995

NIFS-365 K. Itoh, S.-I. Itoh, A. Fukuyama and M. Yagi,
On the Minimum Circulating Power of Steady State Tokamaks; July 1995

NIFS-366 K. Itoh and Sanae-I. Itoh,
The Role of Electric Field in Confinement; July 1995

NIFS-367 F. Xiao and T. Yabe,
A Rational Function Based Scheme for Solving Advection Equation; July 1995

NIFS-368 Y. Takeiri, O. Kaneko, Y. Oka, K. Tsumori, E. Asano, R. Akiyama, T. Kawamoto and T. Kuroda,
Multi-Beamlet Focusing of Intense Negative Ion Beams by Aperture Displacement Technique; Aug. 1995

NIFS-369 A. Ando, Y. Takeiri, O. Kaneko, Y. Oka, K. Tsumori, E. Asano, T. Kawamoto, R. Akiyama and T. Kuroda,
Experiments of an Intense H- Ion Beam Acceleration; Aug. 1995

NIFS-370 M. Sasao, A. Taniike, I. Nomura, M. Wada, H. Yamaoka and M. Sato,
Development of Diagnostic Beams for Alpha Particle Measurement on ITER; Aug. 1995

NIFS-371 S. Yamaguchi, J. Yamamoto and O. Motojima;
A New Cable -in conduit Conductor Magnet with Insulated Strands; Sep. 1995